Eidgenössische Technische Hochschule Zürich

Ecole polytechnique fédérale de Zurich
Politecnico federale di Zurigo
Swiss Federal Institute of Technology Zurich

Compact third order limiter functions for Finite-Volume-Methods

Miroslav Čada and Manuel Torrilhon

Research Report No. 2008-12
May 2008

Seminar für Angewandte Mathematik
Eidgenössische Technische Hochschule
CH-8092 Zürich
Switzerland

Compact third order limiter functions for Finite-Volume-Methods

Miroslav Čada and Manuel Torrilhon

Seminar für Angewandte Mathematik
Eidgenössische Technische Hochschule
CH-8092 Zürich
Switzerland

Research Report No. 2008-12 May 2008

Abstract

We consider finite volume methods for the numerical solution of conservation laws. In order to achieve high-order accurate numerical approximation to nonlinear smooth functions, we introduce a new class of limiter functions for the spatial reconstruction of hyperbolic equations. We therefore employ and generalize the idea of double-logarithmic reconstruction of Artebrant and Schroll [SIAM J. Sci. Comput. 2006].

The result is a class of efficient third-order schemes with a compact three point stencil. The interface values between two neighboring cells are obtained by a single non-linear limiter function. The new methods handle discontinuities as well as local extrema within the standard semi-discrete TVD-MUSCL framework using only a local three point stencil and an explicit TVD Runge-Kutta time marching scheme. The shape preserving properties of the reconstruction are significantly improved, resulting in sharp, accurate and symmetric shock capturing. Smearing, clipping and squaring effects of classical second-order limiters are completely avoided.

Computational efficiency is enhanced due to large allowable Courant numbers (CFL $\lesssim$ 1.6), as indicated by the von Neumann stability analysis. Numerical experiments for a variety of hyperbolic partial differential equations, such as Euler equations and ideal magneto-hydro-dynamic equations, confirm an significant improvement of shock resolution, high accuracy for smooth functions and computational efficiency.

1 Introduction

In the present paper we will derive a new third-order method for the computation of numerical fluxes within the framework of finite volume (FV) schemes for conservation laws. FV methods, in general, are derived from the integral formulation of conservation laws for a spatial domain Ω and a quantity $\boldsymbol{u}$

$$\frac{\mathrm{d}}{\mathrm{d}t}\int_{\Omega}\boldsymbol{u}(x,t)\,\mathrm{d}x = -\int_{\partial\Omega}\boldsymbol{f}(\boldsymbol{u}(x,t))\cdot\boldsymbol{n}\,\mathrm{d}S \tag{1.1}$$

The volume of $\boldsymbol{u}$ can only change in time by the dynamics of the flux $\boldsymbol{f}(\boldsymbol{u}(x,t))$ across the boundary $\partial\Omega$.

Solutions to these equations have typically smooth structures interspersed with discontinuities. An accurate prediction of such interactions is of importance in many computational fluid dynamic (CFD) applications, such as aircraft design, stellar formation, and weather simulations, to name only a few. The main task is to develop algorithms that ensure the conservation property Eq. (1.1), that are highly accurate for smooth regions in both time and space, and have sharp transition where large gradients, discontinuities appear.

Numerical methods for conservation laws can in general be divided into two approaches, a one-step approach, where time and space discretization is coupled via the Cauchy-Kowalenski procedure (see e.g. [10], [18]) and semi-discrete schemes, where time and space integration are separated. The later has been a very successful approach towards the dual objective, i.e. high accuracy and non-oscillatory transitions. It uses strong stability preserving Runge-Kutta time marching schemes, combined with polynomial reconstruction of the interface value $\boldsymbol{u}(x,t)\mid_{\partial\Omega}$ of the flux $\boldsymbol{f}(\boldsymbol{u}(x,t)\mid_{\partial\Omega})$ from a given cell average.

One of the first high-order semi-discrete algorithm was van Leer's TVD-MUSCL (Monotonic Upstream-centered Scheme for Conservation Laws) scheme [13]. A piecewise linear spatial approximation was combined with a second-order time integration. To avoid spurious oscillations total variation diminishing (TVD) limiters were used. TVD-limiters are bounded non-linear functions obeying Harten's TVD conditions [5]. These limiters ensure that any reconstructed values at any time do not lie outside the range of the initial data, thus precluding accurate resolution of local extrema. To avoid this drawback, Harten *et al.* [6] later introduced the concept of essentially nonoscillatory (ENO) schemes. ENO methods use instead of a non-linear limiter an optimal stencil search procedure, which chooses the locally "smoothest" reconstruction, thereby avoiding interpolation across discontinuities. Due to the adaptive stencil, the finally approximated interface value does not consist of all available data. In the weighted ENO (WENO) scheme by Liu *et al.* [11] the interface values are computed as convex combinations of all candidate stencils, hence making better use of the available data. In contrast to TVD-schemes both ENO and WENO methods introduce spurious yet bounded variation, which eventually decreases as the mesh is refined.

At the same time the idea of limiting has been further developed as extensions of the TVD-MUSCL scheme. A third-order method was developed by Woodward and Colella [22]. They used a four-point centered stencil to recover the interface values, which afterwards were limited in the vicinity of a discontinuities. An even higher-order extension was introduced by Suresh and Huynh [17] employing a five-point stencil reconstruction with a limiting procedure, which preserves monotonicity and accuracy for smooth extrema, easing the TVD constrain. To apply the costly limiting routine efficiently, they preprocess the data to localize discontinuities.

In contrast to the method based upon a polynomial approximation of the interface values, Artebrant and Schroll [2] have recently developed a new non-polynomial reconstruction function. Originally motivated by the work of Marquina [12], who used a hyperbola as reconstruction function, they recover the interface values with a local double logarithmic (LDLR) Ansatz function. Due to the logarithmic nature it is able to handle discontinuities without spurious oscillations, yet introducing local bounded variation. In contrast to Marquinas' hyperbolic reconstruction LDLR can recover local extrema without loss of accuracy. It is local, in the sense that it uses only a three-point stencil and it does not use classical limiters to avoid oscillations. Numerical experiment in [2] indicate its superior performance compared to other third-order methods and reconstruction techniques.

Inspired by the results of [2] we have followed a different path. The local and symmetric nature of LDLR allowed a simpler, yet more efficient formulation of Artebrant and Schroll's scheme, thus resembling very much van Leer's three-point TVD-MUSCL algorithm using only a single limiter function. Furthermore this interpretation not only simplified the original reconstruction, but also improved its shock capturing qualities and reconstruction efficiency without the application of a logarithmic function et all. This eventually led to a whole family of limiter functions, which similar to known second-order TVD-limiters exhibit more or less diffusion around discontinuities, yet in contrast to TVD-limiters recover always smooth extrema with third-order accuracy. We want to emphasize, that the paradigm of this paper is to rigorously restrict the limiting procedure to a three-point-stencil. Consequently we have to cope with the problem of recovering discretized smooth structures with few data points. Yet, we remain in the well understood context of the efficient classical TVD-MUSCL scheme. Taking into account that the proposed limiters are simple $(\max -, \min -)$ functions, which do not expand the computational stencil, they become attractive candidates to be easily incorporated into already existing TVD codes.

To emphasize the close relation of the proposed third-order limiting method with van Leer's TVD-MUSCL scheme, we first revisit the second-order one in Section 2. In Section 3, the main properties of the new limiter functions –the key features of our scheme– its connection and the differences to LDLR and other schemes will be explained. Furthermore the difficulty to recover local extrema with a three-point stencil without loss of accuracy will be discussed and solved. In order to reach overall third-order accuracy we use the explicit three stage TVD-Runge-Kutta time integration of [4]. In Section 4. we investigate the characteristic properties of the new methods in the frequency domain, in terms of a linear von-Neumann stability analysis.Convergence studies and various numerical experiments, including one- and two-dimensional systems appear in Section 5. Finally conclusions are presented in Section 6.

2 Spatial reconstruction: standard TVD-MUSCL Methods

For simplicity and in order to settle our notation we consider the numerical approximations to the one-dimensional scalar initial value problem

$$\begin{aligned} u_t &= -f(u)_x, \\ u(x, t=0) &= u_0(x), \end{aligned} \tag{2.1}$$

where u_0 is either a piecewise smooth function with compact support or a periodic function. Note that the flux in Eq. (1.1) and Eq. (2.1) appears on the right hand side to emphasize the semi-discrete formulation. We cover the uniform computational region with control cells $C_i^n = [x_{i-\Delta x/2}, x_{i+\Delta x/2}] \times [t^n, t^{n+1}]$, with $t^{n+1} = t^n + \Delta t$ and the computational grid $x_{i\pm1} = x_i \pm \Delta x$.

Integrating the conservation law Eq. (2.1) over the control volume C_i^n, we obtain the standard finite-volume (FV) update

$$\begin{aligned} \frac{d}{dt}\bar{u}_i &= L_i(\bar{u}^n) \\ &= \frac{1}{\Delta x}\big[\mathcal{F}(\hat{u}^{(-)}_{i-\frac{1}{2}}, \hat{u}^{(+)}_{i-\frac{1}{2}}) - \mathcal{F}(\hat{u}^{(-)}_{i+\frac{1}{2}}, \hat{u}^{(+)}_{i+\frac{1}{2}})\big], \end{aligned} \tag{2.2}$$

for the cell average $\bar{u}_i^n$ at time t^n

$$\bar{u}_i^n = \frac{1}{\Delta x}\int_{x_{i-\Delta x/2}}^{x_{i+\Delta x/2}} u^n(x)\,\mathrm{d}x, \tag{2.3}$$

based on the numerical flux function $\mathcal{F}$, which is supposed to be Lipschitz continuous and consistent with the flux $f(u)$:

$$\mathcal{F}(u, \cdots, u) = f(u). \tag{2.4}$$

The evolution of $\bar{u}_i^n$ is governed by the left and right limits $\hat{u}^{(\pm)}_{i+\frac{1}{2}}$ – the interface values – of the reconstructed function $\hat{u}(x)$. The cell interface value $\hat{u}_{i+\frac{1}{2}} = \hat{u}(\bar{u}_i^n, \bar{u}_{i+1}^n)$ denotes the intermediate value at $x_{i+1/2}$ of the Riemann problem solution with initial data $\bar{u}_i^n, \bar{u}_{i+1}^n$. The calculation of the interface values from the known cell mean values is the essential reconstruction task and determines the scheme's order of accuracy. This is the main concern of this paper.

To obtain higher order accuracy, we have to improve the reconstruction of the left and right limits $\hat{u}^{(\pm)}_{i+\frac{1}{2}}$ and we also have to adjust the time integration by a higher order time-stepping method. Since we consider a local reconstruction, i.e. a three-point stencil, we define the interface values as

$$\begin{aligned} \hat{u}^{(-)}_{i+\frac{1}{2}} &\equiv L(\bar{u}_{i-1}, \bar{u}_i, \bar{u}_{i+1}), \\ \hat{u}^{(+)}_{i+\frac{1}{2}} &\equiv R(\bar{u}_i, \bar{u}_{i+1}, \bar{u}_{i+2}), \end{aligned} \tag{2.5}$$

where capital L and capital R denote the left and right cell interface approximations, respectively. In order to obtain high order non-oscillatory reconstructions, the interpolation function Eq. (2.5) is a priori nonlinear.

The classical second-order TVD-MUSCL scheme assumes a piecewise linear interpolation from the average values $\bar{u}_i(t)$.

$$\begin{aligned} \hat{u}^{(-)}_{i+\frac{1}{2}} &= \bar{u}_i + \frac{\Delta x}{2}\sigma_i \\ \hat{u}^{(+)}_{i-\frac{1}{2}} &= \bar{u}_i - \frac{\Delta x}{2}\sigma_i \end{aligned} \tag{2.6}$$

where the slope σ can either be expressed via downwind, upwind or centered finite differences to recover the Beam-Warmig, Lax-Wendroff or Fromm method, respectively (see e.g [10]).

In order to avoid Gibb's phenomenon and to control the resulting oscillation, TVD-limiters have to be applied directly on the slopes. Hence the reconstructed interface values are expressed in terms of non-linear limiter functions using e.g. the downwind slope

$$\sigma_i = (\frac{\delta_{i+\frac{1}{2}}}{\Delta x})\phi(\theta_i), \tag{2.7}$$

where $\delta_{i+\frac{1}{2}} = \bar{u}_{i+1} - \bar{u}_i$ is the difference across a cell interface, and

$$\theta_i = \frac{\delta_{i-\frac{1}{2}}}{\delta_{i+\frac{1}{2}}}, \quad \delta_{i+\frac{1}{2}} \neq 0 \tag{2.8}$$

is a local smoothness measurement.

If the limiter function satisfies $\phi(1+\Delta x) = 1 + \frac{\Delta x}{2} + \mathcal{O}(\Delta x^2)$ for $\bar{u} \in C^\infty$ and is Lipschitz continuous at $\theta = 1$ we recover second-order accuracy in space. Classical TVD-limiter functions, such as minmod, super-bee, monotonized central difference limiter (MC), etc. (see e.g. [18], [10]) satisfy Harten's TVD-theorem:

$$\begin{cases} 0 \leq \phi(\theta) \leq 2\theta \\ 0 \leq \phi(\theta) \leq 2 \end{cases} \tag{2.9}$$

For $\theta \leq 0$ the reconstruction reduces to the constant cell average itself and smooth extrema for which $\theta \leq 0$ holds can not be recovered accurately. Thus classical second-order TVD schemes are only of second-order away from local extrema and discontinuities. Yet limiter functions which remain inside Harten's TVD region, do not produce any variation in the vicinity of a discontinuity. This property plus their simplicity and efficiency makes them a popular choice for the CFD community. In general limiters can be considered as logical switches. They continuously change from constant to linear reconstruction. The switching argument is the local smoothness measurement Eq. (2.8), which in its simplest form is only the ratio of the left and right slope. Unfortunately classical second-order TVD limiters suffer from several well known drawbacks, such as smearing, clipping and squaring effects of the numerical approximation.

3 Third Order Limiting

In this section we will derive new limiter functions, which are essentially of third-order accuracy and remain in the standard TVD framework. They are based upon a non-linear and non-polynomial reconstruction technique. In addition we will explain the close affinity of quadratic interpolation and limiter-free local double logarithmic reconstruction (LDLR) as proposed by [2].

3.1 Compact Third Order Reconstruction

The TVD-MUSCL scheme adopts a local three-point stencil to get only a linear interpolation for the spatial approximation of a function $g(x)$. Yet three data points are sufficient for constructing a unique quadratic interpolation function

$$p_i(x) = a_i + b_i(x - x_i) + \frac{c_i}{2}(x - x_i)^2$$

resulting in a local third-order reconstruction (see e.g. [6]) of the interface values

$$\begin{aligned} \hat{u}^{(-)}_{i+\frac{1}{2}} &= \frac{5}{6}\bar{u}_i - \frac{1}{6}\bar{u}_{i-1} + \frac{1}{3}\bar{u}_{i+1} \\ \hat{u}^{(+)}_{i-\frac{1}{2}} &= \frac{5}{6}\bar{u}_i - \frac{1}{6}\bar{u}_{i+1} + \frac{1}{3}\bar{u}_{i-1} \end{aligned} \tag{3.1}$$

To derive the parameters a_i, b_i and c_i, the quadratic function $p_i(x)$, integrated over the cell $C_i = [x_{i-\Delta x/2}, x_{i+\Delta x/2}]$ has to recover the cell average $\bar{u}_i$ itself and its left and right derivatives located at cell interfaces have to be approximated to second order.

The oscillatory behavior of the reconstruction depend on a function $g(x)$, which has to be

reconstructed. Assume that $g(x)$ is a smooth function on a spatial domain including the finite control volume $C_i^n = [x_{i-\Delta x/2}, x_{i+\Delta x/2}] \times [t^n, t^{n+1}]$ for all times. Suppose that the lateral derivatives are bounded function of $\mathcal{O}(\Delta x)$. The total-variation inside the control cell for both, linear and quadratic reconstruction is than

$$TV(r_i(x)) = \int_{x_{i-1/2}}^{x_{i+1/2}} |r_i'(x)| \, \mathrm{d}x = \mathcal{O}(\Delta x) \tag{3.2}$$

Here the $r_i(x)$ is representing either a linear or quadratic interpolation function $p_i(x)$.

If the function $g(x)$ is discontinuous inside the control volume C_i^n for any time, one of the lateral derivatives is an unbounded function of $\mathcal{O}(1/\Delta x)$ and the total variation reads

$$TV(r_i(x)) = \mathcal{O}(1). \tag{3.3}$$

Thus to avoid oscillation in the presence of discontinuities we have to either find a different, yet less oscillatory approximation function $r_i(x)$, or apply sophisticated limiters, which diminish the total variation in the vicinity of discontinuities. Since we prefer the second approach, we seek to reformulate Eq. (3.1) similar to Eq. (2.6) using suitable limiters, whose accuracy does not degenerate at local extrema.

3.2 Logarithmic Limiter

Motivated by the work of Marquina [12] on local non-polynomial reconstruction functions, Artebrant and Schroll [2] have recently developed a a local double logarithmic reconstruction (LDLR) using the Ansatz function

$$l_i(x) \sim A_i + B_i \, \ln(x - x_i + C_i) + D_i \, \ln(x - x_i + E_i) \tag{3.4}$$

to approximate the interface values. Identically to the construction of a unique parabola Eq. (3.1) one can construct a local function $l_i(x)$ with uniquely defined values A_i, B_i, C_i and D_i.

The LDLR is, in contrast to Marquina's hyperbolic reconstruction, essentially of third-order away from discontinuities without the explicit use of limiters. Due to the logarithmic nature its total variation scales, in the presence of jump discontinuities, with $\mathcal{O}(\Delta x^q \, |\ln(\Delta x)|)$ [2]. Hence LDLR recovers the cell mean value itself as the mesh is refined. The exponent q will be discussed later. Still a local smoothness measurement as argument of the logarithm has to be built in.

Since LDLR is local and uses only three data point, it turns out that the whole reconstruction procedure can be vigorously simplified and written in a convenient limiter formulation. The complete derivation is shown in Appendix A.

After some algebraic reformulation we finally find

$$\begin{aligned} \hat{u}^{(-)}_{i+\frac{1}{2}} &= \bar{u}_i + \frac{1}{2}\phi(\theta_i)\delta_{i+\frac{1}{2}} \\ \hat{u}^{(+)}_{i-\frac{1}{2}} &= \bar{u}_i - \frac{1}{2}\phi(\theta_i^{-1})\delta_{i-\frac{1}{2}}. \end{aligned} \tag{3.5}$$

This formulation uses only a single limiter function

$$\phi(\theta_i) = \frac{2p((p^2 - 2p\theta_i + 1)\ln p - (1-\theta_i)(p^2-1))}{(p^2-1)(p-1)^2} \tag{3.6}$$

with

$$p = p(\theta_i) = 2\frac{|\theta_i|^q}{1+|\theta_i|^{2q}}. \tag{3.7}$$

In contrast to the TVD-MUSCL scheme, we have to use the limiter also with inverse input and hence also with reverse slopes $\delta_{i\pm\frac{1}{2}}$. This optimizes the use of the local stencil in the TVD-MUSCL framework, resulting in third-order accuracy away from discontinuities. The exponent q in Eq. (3.7) controls the amount of the total variation of the reconstruction. It also appears as an exponent in the convergence estimate of the total variation of LDLR at jump discontinuities.

The limiter function Eq. (3.6) has three removable, yet important singularities at $p(\pm 1) = 1$ and $p = 0$. The first two can be removed by setting $\phi(1) = 1$ and $\phi(-1) = \frac{1}{3}$. This ensures that accuracy is not degenerated at local extrema for which $\theta = \pm 1$ holds. Note that the log-limiter Eq. (3.6) itself is not capable of accurately recovering smooth extrema, due to its singularities. This is also the case in the original LDLR algorithm, where Artebrant and Schroll [2] recommended to interpolate around the singularities using three-data point, thus a parabola. This interpolation would also lead to $\phi(0) = 0$ at $p = 0$.

The shape of the log-limiter function $\phi(\theta)$ is shown in Fig. 1 for different values of q. For

$$q \longrightarrow 0, \quad p(\theta) \longrightarrow 1 \quad \forall \theta \in \mathbb{R} \setminus \{0\}$$

we recover

$$\phi(\theta) = \frac{2+\theta}{3}, \tag{3.8}$$

which indeed is the quadratic reconstruction Eq. (3.1). Note that at the same time the total variation becomes of $\mathcal{O}(|\ln(\Delta x)|)$. Hence it is increasing to infinity as the mesh is refined.

The total variation control parameter q can, in the TVD-MUSCL framework, be also interpreted as a control value of compressibility, similar to the minmod and suberbee limiter. Indeed, the smaller q the more variation is produced in LDLR, introducing spurious oscillations. In other words the function $\phi(\theta)$ moves out of the TVD-region (see Fig. 2, right). The larger q the less variation is produced and discontinuities are smeared out within more cells. This is similar to the transition between the diffusive minmod limiter and the over-compressive suberbee limiter inside Harten's TVD bound. Though for both limiter, minmod and suberbee, variation diminishes in the presence of discontinuity. The non-linear limiter function smoothly extends into the range of $\theta < 0$ and vanishes for $\theta \to \pm\infty$ and $\theta \to 0$, which is essential for limiting discontinuities.

3.3 Simplified Third Order Limiter

The logarithmic limiter $\hat{\phi}(\theta)$ is derived from a double logarithmic Ansatz function, which is conservative, third-order accurate and essentially local variation bounded. The essential characteristics are:

1.) $\phi(1+\Delta x) = 1 + \frac{\Delta x}{3} + \mathcal{O}(\Delta x^m)$ and $\phi(-1+\Delta x) = \frac{1}{3} + \frac{\Delta x}{3} + \mathcal{O}(\Delta x^n)$ with $n, m \geq 2$

2.) $\lim_{\theta\to 0}\phi(\theta) \to 0$ and $\lim_{\theta\to\pm\infty}\phi(\theta) \to 0$

The first condition guaranties a third-order accurate resolution of local extrema, for which holds $\theta = \pm 1 + \Delta x$. The second ensures Eq. (3.6) to be local variation bounded in the presence of discontinuities.

However both, the LDLR and the logarithmic limiter function are complicated and computationally expensive, although Eq. (3.6) has already only one logarithmic evaluation. Furthermore

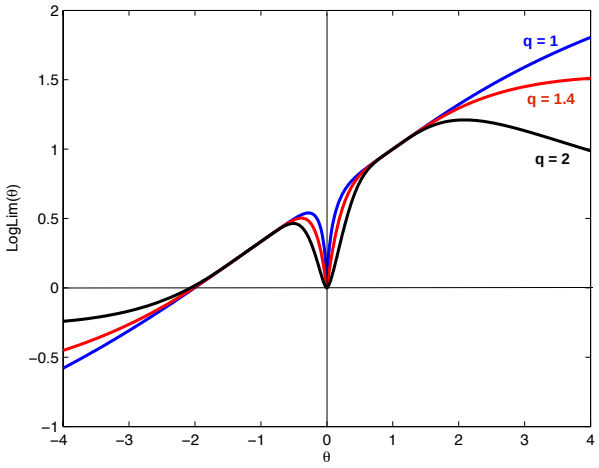

Figure 1: Shape of the limiter function $\phi(\theta)$ Eq. (3.6) for different values of q. For larger q less total variation appears, yet diffusion increases leading to smeared discontinuities.

the LDLR is very sensitive to the paramater q and Artebrant and Schroll [2] suggested to set $q = 1.4$ to ensure stability (see discussion above). Keeping the main features 1.) and 2.) in mind, we can construct a piecewise-linear limiter function with similar properties, yet even improving its shock capturing abilities.

Without the use of a logarithmic function, we not only avoid troublesome singularities but also get better control on the reconstruction routine, thus on the total variation. The new limiter reads:

$$\hat{\phi}(\theta) = \max\Big[0, \min\Big(\frac{2+\theta}{3}, \max\big[-\alpha\,\theta, 0, \min\big(\beta\,\theta, \frac{2+\theta}{3}, \gamma\big)\big]\Big)\Big], \tag{3.9}$$

where the the parameters α, β and γ satisfy the conditions:

$$\begin{cases} 0 \le \alpha \le 2 \\ 1 \le \beta \le 2 \\ 1 \le \gamma \le 2 \end{cases} \tag{3.10}$$

These parameters control the shock capturing properties and total variation of the limiter $\hat{\phi}(\theta)$, similar to the exponent q in Eq. (3.7).

The building block of the new limiter is the quadratic polynomial $\phi(\theta) = \frac{2+\theta}{3}$ from Eq. (3.8). The variables α and β bound the variation of $\hat{\phi}(\theta)$ for $\theta \in (-\infty, 0]$ and $\theta \in [0, 1]$, respectively. The parameter γ represent the upper-bound for the third-order reconstruction for $\theta \in [1, +\infty)$. We bound the variables β and γ according to Harten's TVD-theorem Eq. (2.9). So if we set $\alpha = 0$ we recover a TVD limiter

$$\phi^{TVD}(\theta) = \max\Big[0, \min\Big(2\theta, \frac{2+\theta}{3}, 2\Big)\Big], \tag{3.11}$$

which essentially reconstructs smooth functions, for which $\theta \in [\frac{2}{5}, 4]$, to third-order accuracy. Still degenerating to first-order for smooth extrema in $\theta \le 0$. This function obviously is very economic and simple. Its evaluation only consists of two $(\max, \min)$-statements identical to the minmod-limiter, yet it employs a quadratic polynomial reconstruction as building block. To be able to capture smooth extrema for $\theta \approx -1$ without loss of accuracy, we have to ease

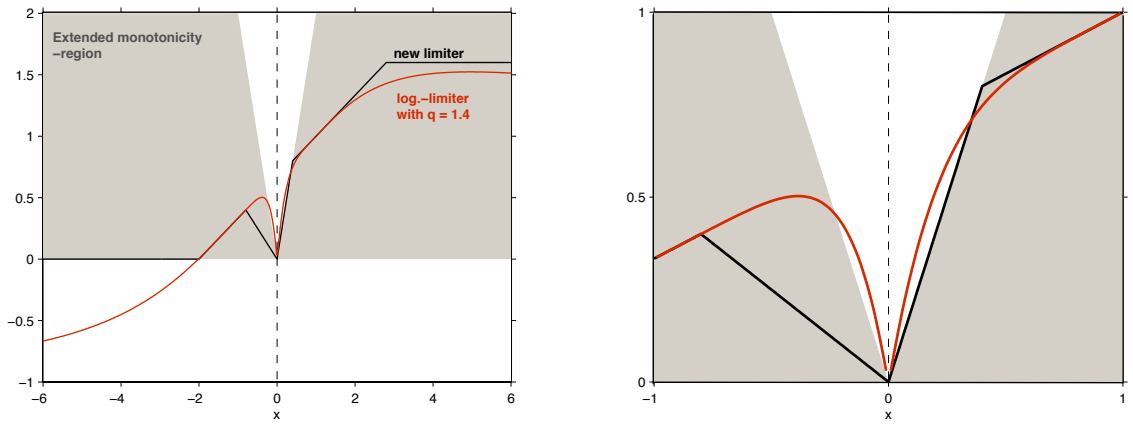

Figure 2: Left: New limiter $\hat{\phi}$ Eq. (3.9) with $\alpha = 0.5, \beta = 2.0$ and $\gamma = 1.6$ matching for logarithmic limiter with $q = 1.4$. Right: Zoom of the inner region. Extended monotonicity-region according to [7].

the monotonicity requirement, i.e. Harten's TVD theorem. Setting $\alpha \geq \frac{1}{3}$ expands the limiter function continuously for $\theta \approx -1$ and allows to recover smooth extrema for $\theta \in [-2, -\frac{2}{3\,\alpha+1}]$ to third-order accuracy.

A further attribute of the proposed limiter is, that it does not satisfy the symmetry requirement of classical second-order TVD limiters

$$\phi(\theta^{-1}) = \phi(\theta)\,\theta^{-1}, \quad \forall \theta \in \mathbb{R} \setminus \{0\}.$$

Suppose the data $\bar{u}^n$ is symmetric in x, we want to impose symmetry on the reconstruction, i.e. $\hat{u}^{(+)}_{i+\frac{1}{2}} = \hat{u}^{(-)}_{i+\frac{3}{2}}$. This requires that the limiter function $\hat{\phi}(\theta)$ satisfy

$$\begin{cases} 1 \leq \hat{\phi}(\theta) \leq \theta\,\hat{\phi}(\theta^{-1}) \leq \theta & \theta \in [1, \infty) \\ \theta \leq \theta\,\hat{\phi}(\theta^{-1}) \leq \hat{\phi}(\theta) \leq 1 & \theta \in (-\infty, 1] \setminus \{0\}, \end{cases} \tag{3.12}$$

which is due to the inverse evaluation of θ in Eq. (3.5).

In Fig. 2 we match the new limiter $\hat{\phi}(\theta)$ with the original logarithmic limiter function $\phi(\theta, q = 1.4)$, Eq. (3.6) and Eq. (3.7). The new limiter $\hat{\phi}(\theta)$ shares the common characteristics of the logarithmic limiter within the simple framework of classical second-order TVD limiters. It is a piecewise linear $(\max, \min)$-function which acts as a logical switch depending on the smoothness measure θ. Its rigorous cutoffs for $\theta \to \pm 0$ (Fig. 2, right) ensure sharp resolution of discontinuous functions, yet remaining in Harten's TVD region for $\theta \geq 0$.

3.4 Geometrical interpretation of the TVD conditions

In the previous section we have derived a new limiter, which reconstructs smooth extrema, for which $\theta \approx \pm 1$ holds, with a quadratic polynomial. Unfortunately in this form, the accuracy of the reconstruction still degenerates to first-order in cells with one vanishing lateral derivative. In the following we will discuss the problem of resolving smooth extrema with limiters for which $\theta \approx \pm 0$ hold.

Let us now consider a non-monotone sinusoidal initial function localized at different time-levels on an equidistant grid. Fig. 3 illustrates the smooth profile as well as the discrete set of cell

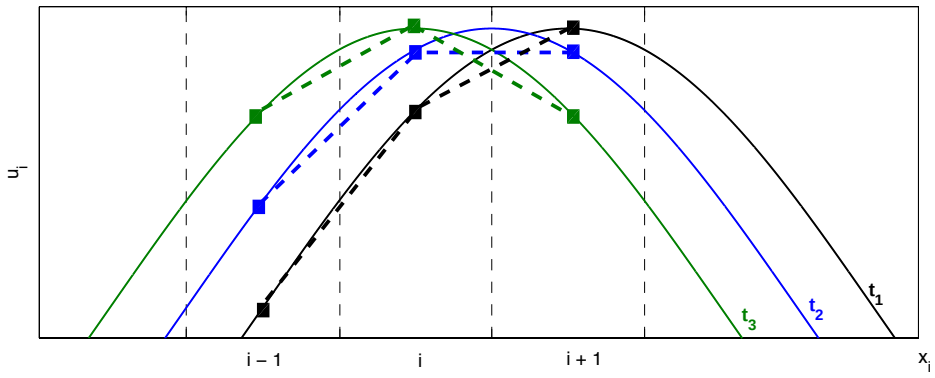

Figure 3: Sketch of a smooth initial profile and its discrete representation at different times, i.e. different locations on a uniform grid.For simplicity we have drawn point values instead of cell mean values.

mean values $\{\bar{u}_{i-1}, \bar{u}_i, \bar{u}_{i+1}\}$, i.e. its discrete representation. The reconstruction of the interface values, based upon the three-cells is shown at three different times. It is obvious that for the times t_2 and t_3, the slope ratio becomes $\theta \leq 0$. Thus limiters satisfying Harten's TVD constrains recover only the cell mean value itself and consequently clip-off local extrema. For t_1, where the data $\bar{u}_i$ are monoton in the interval $[x_{i-1}, x_i, x_{i+1}]$, $\theta \approx 1$ holds and full reconstruction is assured. Using the limiter $\phi^{TVD}(\theta)$ improves the accuracy of the reconstruction only where the data $\bar{u}_i$ are monotone using a quadratic instead of a linear polynomial.

Assume that the lateral slope is given by $\delta_{i-1/2} = \pm\delta_{i+1/2} + \mathcal{O}(\Delta x^\tau)$, with $\tau \in \mathbb{R}$. For smooth data the lateral derivatives are bounded functions $\delta_{i\pm1/2} = \mathcal{O}(\Delta x)$, thus the local smoothness measurement Eq. (2.8) for monotone data yields

$$\theta = \pm 1 + \mathcal{O}(\Delta x^{\tau-1}), \quad \forall \tau \in \mathbb{R}. \tag{3.13}$$

If $\tau > 1$ we have smooth input data and due to condition 1.) in Section 3.3 we reconstruct the interface values to full third order, i.e. $\lim_{\Delta x \to 0} \theta = \pm 1$. For $\tau < 1$ one of the lateral derivatives is an unbounded function with a singularity in the gradient at $\Delta x = 0$. Then the data is discontinuous and we have to limit the reconstruction completely, i.e. either $\lim_{\Delta x \to 0} \theta = \pm\infty$ or $\lim_{\Delta x \to 0} \theta = \pm 0$. Suppose a lateral derivative is a linear function, hence $\delta_{i-1/2} = \pm\delta_{i+1/2} + c\,\Delta x$, with the constant $c \in \mathbb{R}$. Our smoothness criterion yields $\theta = \pm 1 + c$. The constant c represents a measure of curvature for a function between two neighboring cells. For a rather large constant $|c|$ the discretized input data, especially on a coarse grid, represent a discontinuity rather than a smooth function. Consequently such data has to be fully limited. Note that for steep, narrow extrema $|c|$ will also be large and a fine resolution is needed to accurately reconstruct these extrema with only three-data points.

The characteristic of a limiter to reconstruct linear functions with a large constant $|c|$ is often referred to as over-compressibility. It is controlled by the limits of Harten's TVD conditions Eq. (2.9), especially by the lower bound $\phi(\theta) \leq \beta\,\theta$ with $1 \leq \beta \leq 2$ (see Eq. (3.10)). Choosing a smaller limit $\phi(\theta) = \theta$ yields a more diffusive limiter, such as the minmod function. Increasing the bound to $\phi(\theta) \leq 2.5\,\theta$, the limiter is outside Harten's TVD region, but it reconstructs steeper transitions, i.e. linear function with a "larger" constant $|c|$, to full third-order. This is the case for the logarithmic limiter Eq. (3.6) of the LDLR reconstruction as can be seen clearly in Fig. 2 (right picture). But it also leads to spurious over and undershoots, since the limiter is outside TVD bounds. This is the reason why we choose the lower limit to be inside the TVD region. If

the constant $|c|$ is small, for shallow gradients, we have $\theta \approx 1$ and we yield third-order recovery.

To be able to recover smooth extrema with different signs of the lateral derivatives, i.e. $\theta = -1$, the monotonicity condition has to be soften. The extended monotonicity region, Fig. 2), is indicating a domain where the resulting interpolant, i.e. the reconstructed values are monotone, even though the data is not necessarily monotone (Fig. 3 for t_3). Although we have already extended here the limiter $\hat{\phi}(\theta)$ for $\theta < 0$, we can only fully reconstruct local extrema which are almost perfectly symmetric at the cell center u_i and therefore its slopes $\delta_{i\pm1/2}$ are of same absolute value but different signs ($\theta \approx -1$). As shown in Fig. 3 this is a very artificial case, since local extrema although initially located at a cell center, will eventually be relocated during their evolution inside the cell.

It is crucial to understand, that although the LDLR algorithm is of third-order, the derived logarithmic limiter Eq. (3.6) and also its simplification Eq. (3.9) suffers from accuracy lost at local extrema for which $\theta \to 0$ or $\theta \to \pm\infty$. Hence smooth extrema with one vanishing lateral derivative are always limited instead of being fully reconstructed. Fig. 3, for t_2.

In order to overcome this drawback we have to extend the new limiter formulation. For this we have introduced an asymptotic region based on the indicator function

$$\eta(\delta_{i-1/2}, \delta_{i+1/2}) = \frac{\delta_{i-1/2}^2 + \delta_{i+1/2}^2}{(r\,\Delta x)^2} \tag{3.14}$$

which is a function of the lateral derivatives $\delta_{i\pm1/2}$, instead of θ. In addition it depends on the grid size Δx and a dimensionless constant $r \in \mathbb{R} \setminus \{0\}$. We will refer to the constant r as radius of the asymptotic region.

For $\eta \leq 1$ the lateral derivatives $\delta_{i\pm1/2}$ are to small for θ being a good measure for discontinuities. For $\eta > 1$, $\delta_{i\pm1/2}$ are large enough so that the limiter $\hat{\phi}(\theta)$ can be applied. In Fig. 4 one can see that the asymptotic region spans a circle around $\theta \approx \pm 0$ with the radius r. Thus data which is inside this domain is reconstructed to full third-order, whereas data outside the asymptotic region is passed to the limiter $\hat{\phi}(\theta)$ Eq. (3.9).

To investigate the meaning of η for continuous data with a vanishing derivative we first expand the lateral derivatives $\delta_{i\pm1/2}$ around $u'(x_{i-1/2})$:

$$\delta_{i-1/2} = u'(x_{i-1/2})\Delta x + \frac{1}{12}u'''(x_{i-1/2})\Delta x^3 + \mathcal{O}(\Delta x^4) \tag{3.15}$$

$$\delta_{i+1/2} = u'(x_{i-1/2})\Delta x + u''(x_{i-1/2})\Delta x^2 + \frac{7}{12}u'''(x_{i-1/2})\Delta x^3 + \mathcal{O}(\Delta x^4)$$

Assuming a local extrema $u'(x_{i-1/2}) = 0$, $u''(x_{i-1/2}) \neq 0$ and cancelling higher order terms, Eq. (3.14) yields

$$\eta(\delta_{i-1/2}, \delta_{i+1/2}) = \left(\frac{u''(x_{i-1/2})}{r}\right)^2 \Delta x^2. \tag{3.16}$$

Thus the function η is a measure of the second derivative, i.e. of the curvature of the data. Note that $\eta = \mathcal{O}(\Delta x^2)$ which is smaller than the required linear convergence of η for a third-order reconstruction. In this perspective the quadratic convergence is optimal, since one can not expect more from a three-point stencil.

Considering the case of smooth extrema with one vanishing lateral in the discrete FV-setting, i.e. $\delta_{i+1/2} = 0$ and $\delta_{i-1/2} = c\,\mathcal{O}(\Delta x^{\tau})$ with $c \in \mathbb{R}$. The asymptotic region η becomes

$$\eta(0, c\,\mathcal{O}(\Delta x^{\tau})) = \left(\frac{c}{r}\right)^2 \mathcal{O}(\Delta x^{2(\tau-1)}). \tag{3.17}$$

Similar to the previous discussion $\lim_{\Delta x \to 0} \eta = 0$ for $\tau > 1$ and consequently we are inside the asymptotic region, i.e. third order reconstruction. For $\tau < 1$ we are outside the asymptotic region and hence complete limiting is applied. If $\tau = 1$, Eq. (3.17) yields

$$\eta(0, c) = \left(\frac{c}{r}\right)^2.$$

Remember we consider functions inside the asymptotic domain $\eta \leq 1$ as smooth. For $\frac{c}{r} \leq 1$ we are inside and for $\frac{c}{r} > 1$ outside the asymptotic region. Thus the parameter r plays a significant role for bounded function of $\mathcal{O}(\Delta x)$. As mentioned before, we do not have any analytical possibility to estimate the size of the constant $|c|$. Heuristically a "large" $|c|$ might indicate discontinuous data, whereas one could expect a smooth function to have a slighter curvature, i.e a "smaller" $|c|$. It is important to understand that playing with the constant r, i.e. increasing or decreasing the size of the asymptotic domain clearly affects the amount of introduced variation. Yet the function η only affects region with one vanishing lateral derivative. Since for discontinuous data, say e.g. $\tau = -1$ we get

$$\eta(0, c\,\mathcal{O}(\Delta x^{-1})) = \left(\frac{c}{r}\right)^2 \mathcal{O}(\Delta x^{-4}),$$

hence fourth-order convergence towards infinity. Thus switching to the limiter $\hat{\phi}(\theta)$ already on a coarse grid in the presence of a jump discontinuity. It is clearly faster than the convergence order of total variation for LDLR $\mathcal{O}(\Delta x^{1.4}\,|\ln(\Delta x)|)$ [2] and $\mathcal{O}(\sqrt{\Delta x})$ for Marquina's hyperbolic reconstruction [12]. This is the reason why Marquina has to preprocess the lateral derivatives to avoid spurious oscillation in the presence of jump discontinuities.

Finally our new third-order limiter function reads:

$$\phi^{\mathcal{O}(3)}(\delta_{i-1/2}, \delta_{i+1/2}) = \begin{cases} \frac{2+\theta}{3} & \text{if } \eta \leq 1-\epsilon \\ \hat{\phi}(\theta) & \text{if } \eta \geq 1+\epsilon \\ \frac{1}{2}\left(\left(1 - \frac{\eta-1}{\epsilon}\right)\frac{2+\theta}{3} + \left(1 + \frac{\eta-1}{\epsilon}\right)\hat{\phi}(\theta)\right) & \text{else} \end{cases} \tag{3.18}$$

with ϵ being a small positive number, which is about the size of the particular machine precision and ensures Lipschitz continuity for $\phi^{\mathcal{O}(3)}$. Note that in the proposed limiter, the problem of accurately recovering smooth extrema with one vanishing lateral derivative and simultaneously reconstructing sharp gradients is rigorously decoupled. Consequently, in the presence of a discontinuity the new limiter yields $\phi^{\mathcal{O}(3)} \longrightarrow \hat{\phi}(0) = 0$ with $\mathcal{O}(\Delta x^4)$. This convergence rate towards zero total variation is of several magnitudes higher than that of Artebrant and Schroll's double logarithmic reconstruction or Marquina's hyperbolic reconstruction.

Fig. 4 points out the characteristic properties of the final limiter Eq. (3.18). It is, because of simplicity, more a sketch rather than an actual plot of the function $\phi^{\mathcal{O}(3)}$. This way we can geometrically clarify the asymptotic region η, a confidence region and a transition domain.In the first two regions the interface values are reconstructed to full third-order, since we are "confident" that the input data is smooth, i.e. $\tau > 1$ and $\frac{c}{r} \leq 1$ in Eq. (3.17). Whereas in the transition region the discretized input data is discontinuous. In other words $\tau < 1$ or $\frac{c}{r} \gg 1$ in

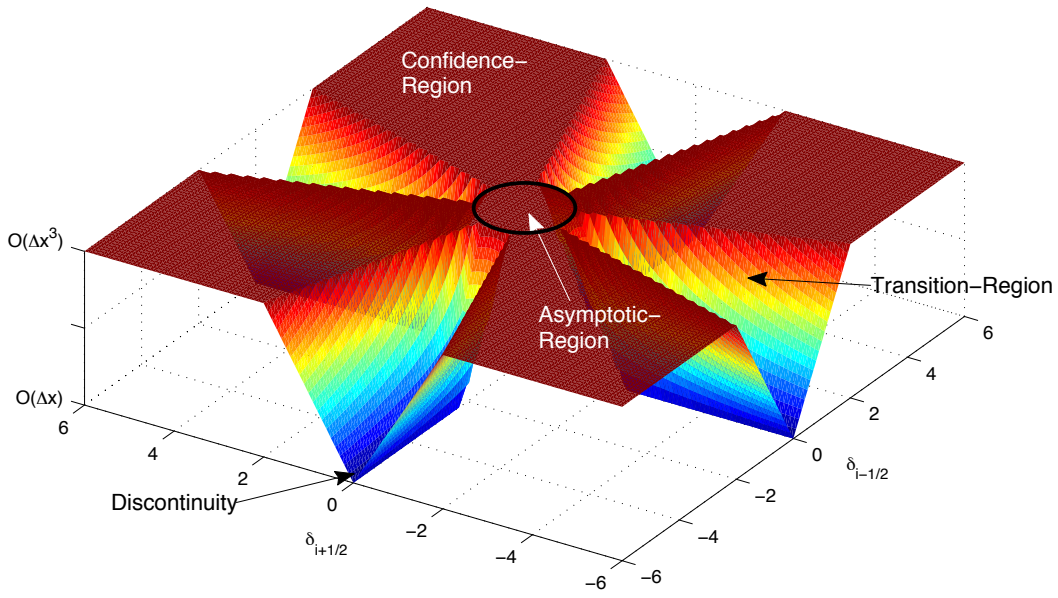

Figure 4: Sketch of new limiter function including the asymptotic region for smooth extrema with one vanishing lateral derivative $\delta_{i\pm1/2}$. Red color indicates third order recovery.

Eq. (3.17) and consequently the data has to be fully limited. The lower $(1-\epsilon)$ and upper limit $(1+\epsilon)$ of the dark circle around the asymptotic region ensure Lipschitz continuity of $\phi^{\mathcal{O}(3)}$ and so for the numerical flux function $\mathcal{F}$ in Eq. (2.2). away from the asymptotic domain cuts along constant $\delta_{i-1/2}$ correspond to the limiter function Fig. 2.

We want to emphasize that the asymptotic region only affects smooth functions with one vanishing lateral derivative and is decoupled from the shock capturing limiter $\hat{\phi}(\theta)$. Once $\eta > 1+\epsilon$ the function $\hat{\phi}(\theta)$ is switched on. This limiter, as discussed before, satisfies at least for $\theta > 0$ Harten's TVD constrains, thus not producing variation at all. Note that numerical experiments indicate, that the region for $\theta < 0$ is very seldom evaluated, namely when the smooth extrema is precisely located at the cell center. Most of the time the cells for which $\theta \approx \pm 1$ holds are affected. From the reconstruction point of view, this means that these cells have to be identified as fast as possible, when refining cell size Δx. Therefore the choice of the radius r is crucial. This variable, at least on a coarse grid, contolls the compressibility of η Eq. (3.16), Eq. (3.17), respectively. It sets the limit on the curvature of the data, which still is considered as smooth. This is critical since discretized shallow gradient or smooth extrema eventually have identical curvature for a certain grid size Δx. Because of this we recommend, especially for large jump discontinuities and coarse grids, to set $r \in [0.001, 1]$. However numerical experiments using a diffusive numerical flux function indicate that $r > 1$ is possible and for certain examples favored. This compromise is the ultimate, independent of the reconstruction ansatz function, for a local three-point-stencil.

4 Time Integration

Since numerical errors in time and space dicretisation can be swapped, we need to adjust the time marching scheme. Third-order in time is accomplished by integrating the finite volume update Eq. (2.2) using the explicit third-order TVD Runge-Kutta method of [4].

This specific Runge-Kutta scheme consists of a three times repeated application of a single Euler's step

$$\boldsymbol{u}^{n+1} = \boldsymbol{u}^n + \Delta t\, \boldsymbol{L}\, \boldsymbol{u}^n = \boldsymbol{M}(\Delta t\, \boldsymbol{L})\, \boldsymbol{u}^n. \tag{4.1}$$

This is a system of explicit linear equations with the matrix operator $\boldsymbol{L}$ containing the non-linear spacial approximation for the discrete set of values $\boldsymbol{u}^{n+1} \equiv \{u_i^{n+1}, n = \dots 0, 1, 2, \dots\}$, i.e. $\boldsymbol{L}\, \boldsymbol{u}^n = L_i(u^n)$.

For the explicit Euler time marching scheme the operator $\boldsymbol{M}$ reads

$$\boldsymbol{M}(\Delta t \boldsymbol{L}) = \boldsymbol{I} + \Delta t\, \boldsymbol{L}, \tag{4.2}$$

and for the explicit thee-stage Runge-Kutta-method

$$\boldsymbol{M}(\Delta t\, \boldsymbol{L}) = \boldsymbol{I} + \Delta t\, \boldsymbol{L} + 1/2(\Delta t\, \boldsymbol{L})^2 + 1/3(\Delta t\, \boldsymbol{L})^3. \tag{4.3}$$

Note $\boldsymbol{M}$ is a polynomial in the spacial operator $\Delta t\, \boldsymbol{L}$.

To investigate the linear stability of the algorithm we assume $\boldsymbol{L}$ to be linear. We consider the time evolution of a sinusoidal grid function in an unbounded domain, with $a > 0$ governed by the scalar linear advection equation

$$u_t + a\, u_x = 0, \quad u_k(x, 0) = v_k(0)\, e^{\boldsymbol{i}\, k\, x}, \quad x \in (-\infty, \infty). \tag{4.4}$$

where $v_k(t)$ is the Fourier transform of the exact solution, $k = 2\,\pi/\lambda$ is the wave number and $\boldsymbol{i}$ represent the imaginary unit. Discretizing Eq. (4.4) on a grid with uniform spacing Δx we can calculate the complex amplitude, i.e the amplification factor of a numerical scheme

$$\frac{v_k^{n+1}}{v_k^n} = \boldsymbol{M}(\Delta t\, \hat{L}(k)) \equiv z(k), \tag{4.5}$$

where $\hat{L}(k) = \lambda_k$ are the eigenvalues of the spatial operator $\boldsymbol{L}$. This amplification factor is an approximation of the amplification factor of the exact advection equation Eq. (4.4):

$$z^{ex}(k) = \frac{u_k(x, \Delta t)}{u_k(x, 0)} = e^{-\boldsymbol{i}\, \nu\, k\, x}, \tag{4.6}$$

with the CFL number

$$\nu = \frac{a\, \Delta t}{\Delta x}. \tag{4.7}$$

Numerical stability, in the von Neumann sense, implies that the absolute value of the amplification factor $z(k)$ should not exceed unity. Hence the characteristic equation for the explicit third-order Runge-Kutta method reads

$$|z(k)| = |1 + \Delta t\, \lambda(k) + \frac{1}{2}(\Delta t\, \lambda(k))^2 + \frac{1}{3}(\Delta t\, \lambda(k))^3| \leq 1. \tag{4.8}$$

Applying the quadratic reconstruction Eq. (3.1) to the advection equation, we yield the semi-discretization

$$\frac{d}{dt}\, u_i = -a \left(\frac{3u_i + u_{i-2} - 6u_{i-1} + 2u_{i+1}}{6\Delta x} \right), \tag{4.9}$$

which corresponds to the complex spectrum

$$\Delta t\, \lambda_k = -\frac{1}{6} \nu\, e^{-\boldsymbol{i}\, k\, \Delta x} (e^{\boldsymbol{i}\, k\, \Delta x} - 1)(5 + \cos(k\, \Delta x) + 3\boldsymbol{i}\, \sin(k\, \Delta x)) \tag{4.10}$$

Inserting Eq. (4.10) into the characteristic equation of the explicit third-order Runge-Kutta method Eq. (4.8) yields the amplification factor of the Fourier mode. To obtain the amplification factor for the above scheme Eq. (4.9) with a second-order time marching method, we have to drop $\mathcal{O}((\Delta t\,\lambda(k))^3)$ in Eq. (4.8).

Fig. 5 shows the absolute value of the amplification factor plotted against the reduced wave number $\tilde{k} = k\,\Delta x$ for different CFL numbers ν. The left figure represents an explicit second-order time integration and the right one represents the three-stage Runge-Kutta time marching scheme for Eq. (4.4). Both plots indicate that the scheme Eq. (4.9) is less dissipative for very small Courant numbers $|\nu| \leq 0.1$. However using the third-order time integration, the dissipation of high frequency waves gets reduced with large Courant numbers $|\nu| \geq 1.0$. Furthermore the third-order time marching scheme, in contrast to the second-order one, gets unstable for high frequency waves, but remains stable for small frequencies. The Fourier modes in the solution have in general the largest amplitude at low wave numbers.

From the numerical evaluation of the wave spectrum, we conclude that the explicit three-stage TVD Runge-Kutta method is stable for all values of the Courant number $|\nu| \leq 1.63$. Note that using only a second-order time marching scheme plus the third-order spatial reconstruction we would obtain a more restrictive CFL condition $|\nu| \leq 0.83$.

Using a classical truncation error analysis in the frequency domain, we can recover the formal order of accuracy of the scheme. We consider the ratio of the numerical amplification factor and the exact one:

$$\mathcal{R}(\tilde{k}) = \frac{z(\tilde{k})^{nu}}{z(\tilde{k})^{ex}}. \tag{4.11}$$

With a standard Taylor expansion we get for the third-order method Eq. (4.9) combined with a three-stage Runge-Kutta time integrator

$$\mathcal{R}(\tilde{k})^{\mathcal{O}(3)} - 1 = -\frac{1}{24}\,\nu(2+\nu^3)\tilde{k}^4 + \mathcal{O}(\tilde{k}^5). \tag{4.12}$$

The ratio of the amplification factors for the third-order scheme $\mathcal{R}(\tilde{k})^{\mathcal{O}(3)}$ approximates 1 to fourth-order $\mathcal{O}(\tilde{k}^4)$. The leading term is a real number which is associated with a diffusive character of the method. Comparing this quantity with only a second-order time marching scheme and the quadratic reconstruction Eq. (4.9) we obtain

$$\mathcal{R}(\tilde{k})^{\mathcal{O}(2)} - 1 = -\frac{1}{6}\boldsymbol{i}\,\nu^3\,\tilde{k^3} - \frac{1}{24}\nu(2-3\nu^3)\tilde{k^4} + \mathcal{O}(\tilde{k}^5). \tag{4.13}$$

This scheme is formally only of second-order accuracy $\mathcal{O}(\tilde{k}^3)$ with a dispersive character.

In Fig. 6 we compare numerical results for the linear advection equation Eq. (4.9). Two different time integration schemes, namely the second-order Heun and the three-stage Runge-Kutta method, are used. The unlimited third-order algorithm produces only small, yet symmetric and local, over and undershoots. The oscillation decay in time, since diffusion is dominant. In contrast, the second-order scheme with third-order spatial accuracy is dispersive and the oscillations disperse as time proceeds and completely destroy the shape of the initial profile.

We are aware that the von Neumann analysis gives only a sufficient condition for stability for linear operators $\boldsymbol{L}$. Our reconstruction is based upon a non linear limiter function. Its behavior in the frequency domain can not be completely represented by a linear stability analysis. Yet the

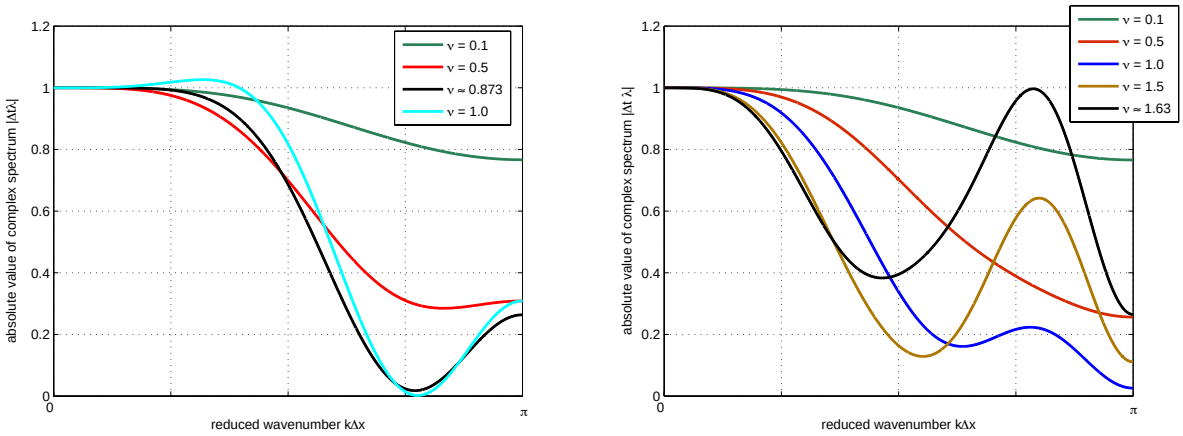

Figure 5: Stability region of explicit second-order (left) and explicit third-order (right) Runge-Kutta method time integration combined with quadratic spatial reconstruction. CFL-condition for second-order $|\nu| \leq 0.83$, third-order $|\nu| \leq 1.63$ time-marching.

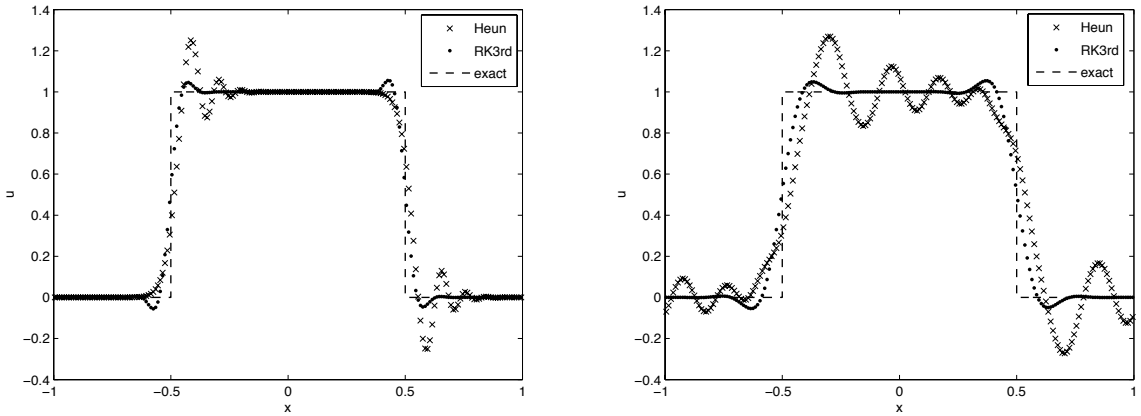

Figure 6: Linear advection of a square wave: unlimited quadratic reconstruction with a second-order (red) and third-order (black) TVD time marching scheme, until $t = 2$ (left) and $t = 20$ (right), $\nu = 0.8$ with 200 cells.

analysis indicates the benefits using a three-stage Runge-Kutta time integration together with third-order spatial reconstruction. We not only obtain a far less restrictive CFL condition than using a second-order time marching scheme, we also improve its dissipative character especially for high frequency waves and its shape preserving properties. Moreover due to the local character of the oscillations, the non linear limiter function will only be limiting few cells around a discontinuity. Whereas in the second-order, dispersive, algorithm the limiter has to be applied on all cells to stabilize the computation.

5 Numerical Experiments

In this section we conduct a series of convergence and accuracy tests from one-dimensional linear advection equation to two-dimensional Euler equations including also a pseudo convergence test for the one-dimensional ideal MHD equations.

5.1 One-dimensional Scalar Equations

We solve the scalar linear advection equation

$$u_t = -u_x, \quad u(t=0,x) = u_0(x), \tag{5.1}$$

with different initial conditions on a periodic domain $x \in [-1,1]$.

5.1.1 Convergence studies for a smooth initial profile

We consider the initial conditions $u_0(x) = \sin(\pi\, x)$ and solve the advection equation Eq. (5.1) for different radii r of the asymptotic region Eq. (3.14). Rather than presenting a table with the convergence rates calculated between two consecutive results, we have plotted in Fig. 7 the computed L_1- and L_∞-errors obtained at $t = 1$ with Courant number $\nu = 0.9$. The discrete norms are given by:

$$\begin{aligned} ||e(\cdot,t^n)||_{L_1} &= \Delta x \sum_{i=1}^{N} |\bar{u}(x_i,t^n) - \bar{u}_i^n| \\ ||e(\cdot,t^n)||_{L_\infty} &= \max_{1\le i\le N} |\bar{u}(x_i,t^n) - \bar{u}_i^n| \end{aligned} \tag{5.2}$$

Here N is the number of computational cells. In this way we get a clear impression when –in terms of spatial resolution and radius r– the designated error, i.e. the error of the unlimited quadratic polynomial reconstruction is reached. We have to keep in mind that no FV-reconstruction based on three cells can be more accurate than the pure quadratic polynomial reconstruction. Calculating the convergence rate between two consecutive results gives in all three cases, $r = 1.0$, $r = 0.1$ and $r = 0.01$, the formal third-order using only 40 cells. However it is obvious that the designated accuracy is only reached with more cells, especially for a small asymptotic region $r \le 0.01$. Note that the curvature of our initial function is $|u''(x)| = \pi^2$. Whereas Artebrant and Schroll [2] use the initial function $u_0(x) = 1.0 + 0.2\,\sin(\pi\, x)$ with smaller curvature $|u''| = 0.2\pi^2$. Consequently they recover third-order convergence rate setting the variational-control-parameter $q = 1.4$ (see Eq. (3.6) and Eq. (3.7)) with 40 grid cells. Using the same initial data we recover the desired convergence error for $r = 1.0$ with only 10 cells, hence faster. This is due to the fact that $\eta = \mathcal{O}(\Delta x^2)$ for smooth extrema.

Fig. 8 shows two different solutions of the advection equation: one obtained with step function and once with a sin-wave as initial function $u_0(x)$. The picture clearly points out the effect of the asymptotic region for different radii r. Choosing a small radius $r \le 0.01$, the limiter needs a sufficient resolution, around 200 cells, to be able to distinguish between a discretized smooth extrema or a shallow gradient. Note that the two profiles are advected ten times ($t = 20$) around the domain $x \in [-1,1]$. We can also observe, that even for a large asymptotic region, essentially no limiting, the method does not become unstable, unlike an unlimited second-order TVD-method. The over-and under-shoots remain localized and do not grow with time.

5.1.2 Initial Condition with Discontinuities

We take a test case, proposed in [8]. It consists of a tight combination of four waves, namely a smooth, but narrow Gaussian peak, a square wave, a triangle wave and a half ellipse. The triangle has a smooth transition at its bottom. We use periodic boundary conditions on the domain $x \in [-1,1]$ and the initial profile is advected until $t = 20$.

In Fig. 9 we compare our new limiter function $\phi^{\mathcal{O}(3)}$ (LimO3) with third-order ENO method

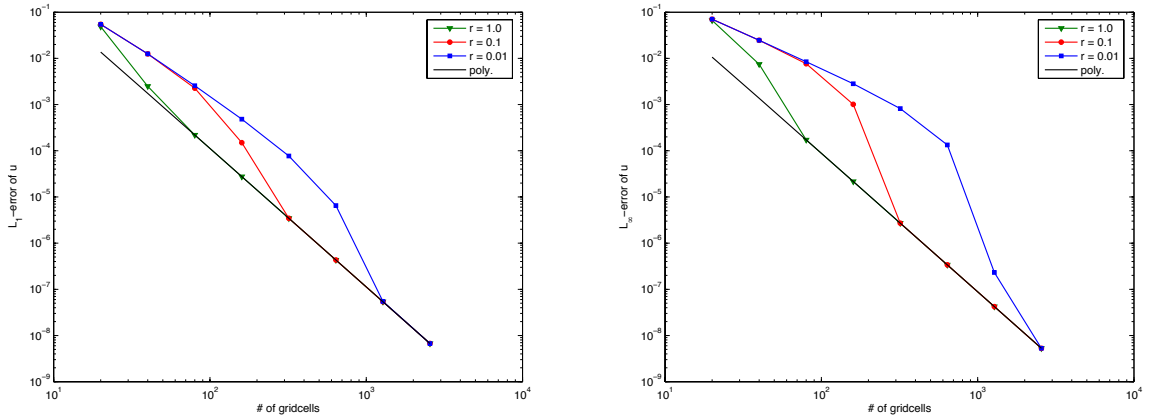

Figure 7: Double logarithmic plots of the empirical order of convergence (EOC) for the advection equation with $u_0(x) = \sin(\pi\, x)$ at $t = 1$ with $\nu = 0.9$. Solution for different radii r of the asymptotic region (3.14) are shown.

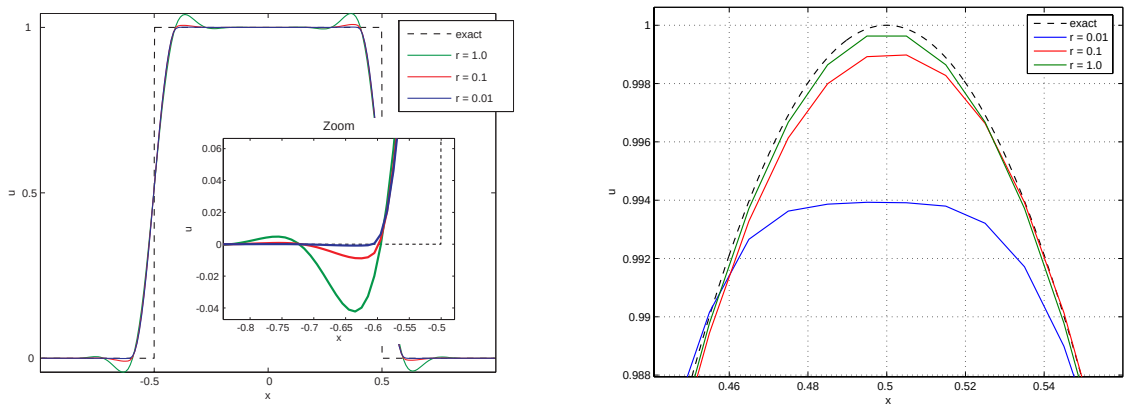

Figure 8: Solution of the advection equation with a square wave (left) and a sin-wave (right) as initial conditions. Results are calculated at $t = 20$ with $\nu = 0.8$ using 200 cells for different expansion of the asymptotic region.

(ENO3) and with LDLR. ENO3 is essentially not local since it uses a five point stencil to choose between the "smoothest" reconstruction for the interface values. All schemes use the same explicit third-order Runge-Kutta method for time integration. Since our method has a less restrictive CFL condition, we run the experiment with $\nu = 0.8$, instead of $\nu = 0.6$ for ENO3 and LDLR.

Especially in contrast to the classical TVD-MUSCL scheme (see e.g. [3]), the new method gives a good approximation of the exact profile. Typical drawbacks of second-order TVD limiter, such as smearing and squaring of linear waves are completely avoided. The results are perfectly symmetric and corners a very well resolved. The symmetry of the results is probably due to the fact, that near $\theta = 1$ we recover a smooth function of second degree. Whereas second-order TVD limiters, such as superbee or minmod, are only Lipschitz continuous near $\theta = 1$. This drawback enhances the probability, that the wrong choice of slopes is used for the one-sided approximation.

Both LimO3 and LDLR are essentially of the same quality, yet LimO3 has a higher Gaussian peak and produces less overshoots for the half ellipse. Whereas ENO3 is not able to distin-

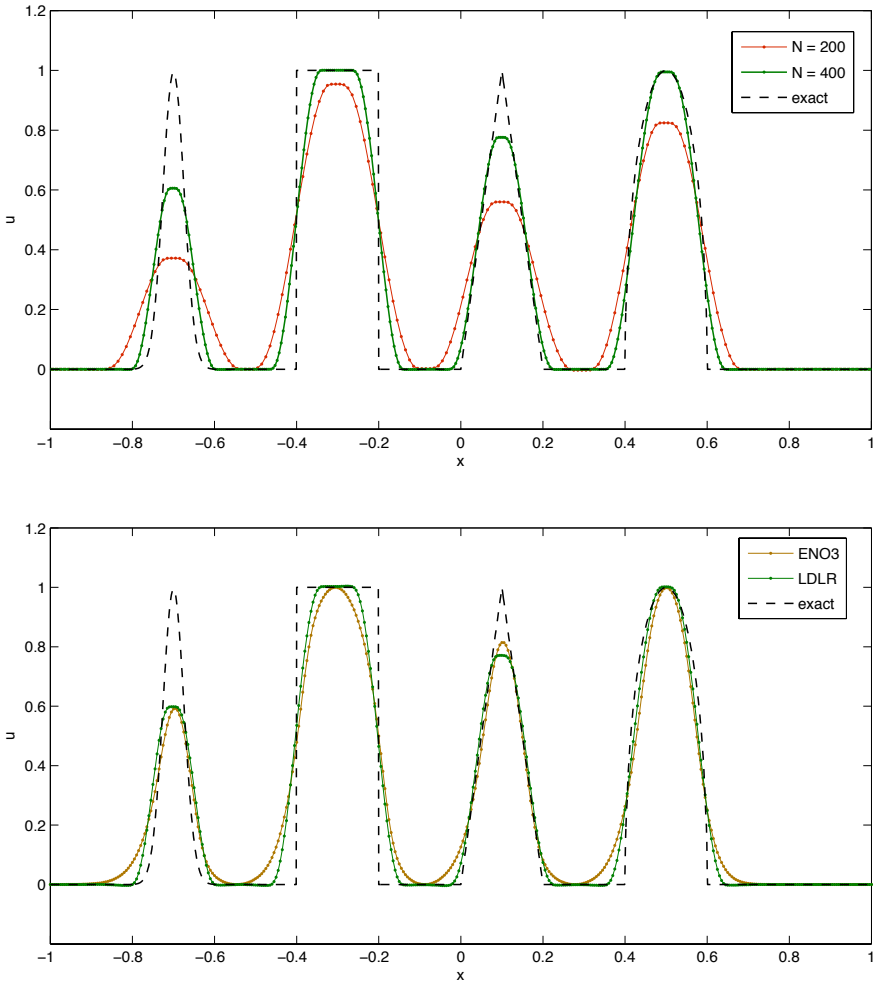

Figure 9: Advection of discontinuities with $\nu = 0.8$ until $t = 20$. Top profile: Proposed method LimO3 on 200 and 400 cells with the radius $r = 0.01$. Bottom profile: LDLR and ENO3 taken from [2] on 400 cells with $\nu = 0.6$.

guish between the different waves and always produces sinusoidal-like wave patterns. All three method produce negative values, yet for LimO3 they are of a smaller magnitude. Remember the asymptotic region scales, in the presence of jump discontinuities, with $\mathcal{O}(\Delta x^4)$.

5.1.3 Nonlinear Scalar Equations

It is our aim to examine the total variation for nonlinear scalar equations. First we solve the Burger's equation

$$u_t = -\left(\frac{u^2}{2}\right)_x, \quad u_0(x) = 1 + \frac{1}{2}\sin(\pi(x-1)) \tag{5.3}$$

on a periodic domain $x \in [-1, 1]$ under CFL condition $\nu = 0.9$.

Second we calculate the non-convex and Buckley–Leverett equation

$$u_t = -\left(\frac{u^2}{u^2 + a(1-u)^2}\right)_x, \quad u_0(x) = \begin{cases} 1 & \text{if } -\frac{1}{2} \le x \le 0 \\ 0 & \text{elsewhere} \end{cases} \tag{5.4}$$

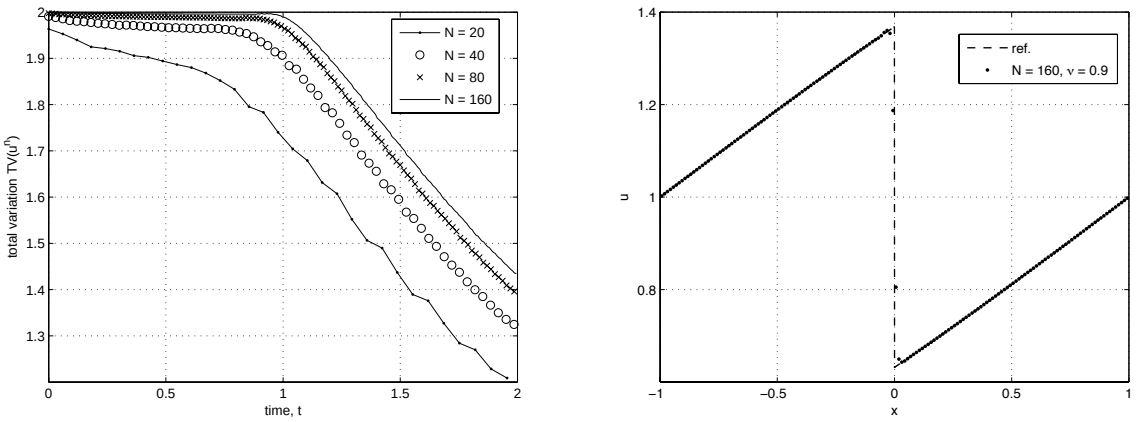

Figure 10: Total variation of Burger's equation (left) and LimO3 approximation with $\nu = 0.9$ and $r = 0.1$ at $t = 2.0$

on the same spatial domain and with the Courant number $\nu = 0.7$. The constant a is set to $\frac{1}{4}$ and the initial profiles are taken from [2]. For the Buckley–Leverett equation we use the local-Lax-Friedrichs flux

$$\mathcal{F}_{i+\frac{1}{2}}(\hat{u}^{(-)}, \hat{u}^{(+)}) = \frac{1}{2}\left(f(\hat{u}^{(-)}) + f(\hat{u}^{(+)}) - a_{i+1/2}(\hat{u}^{(+)} - \hat{u}^{(-)})\right), \tag{5.5}$$

with the wave propagation speed $a_{i+1/2} = \max\left(|\frac{\partial f(u)}{\partial u}|\right)$.

We calculate for both equations the total variation for a grid function $\bar{u}$

$$TV(\bar{u}^n) \equiv \sum_{i=1}^{N} |\bar{u}_{i+1}^n - \bar{u}_i^n| \tag{5.6}$$

of the discrete solution.

Fig. 10 (left) points out the numerical behavior of the total variation for the Burger's equation and the LimO3 approximation at $t = 2.0$. We observe that the calculated total-variation is bounded by $TV(\bar{u}^0)$ and gradually decreases with time as a jump discontinuity forms at $t \approx 1.0$. In contrast to LDLR the accuracy of the solution with 40 cells is significantly better (see [2]) and the evolving smooth profile for $t \in [0, 0.8]$ is recovered accurately. Note that for all three resolutions the value of total variation before shock forms is always larger than of LDLR. Hence the smooth profile is resolved more accurately with few computational cells. This could even be improved with a larger asymptotic region, yet also leading to larger, but bounded spurious oscillations shortly before the jump discontinuity forms. However once the discontinuity clearly appears the limiter yields $\phi^{\mathcal{O}(3)} \longrightarrow \hat{\phi}(0) = 0$ and the oscillations completely disappear.

In the case of Buckley–Leverett equation we analyze a very similar total-variation behavior (see Fig. 11). Although we introduce some spurious variation, which eventually diminishes as the mesh is refined. The slight overshoots at $x = 0.62$ in the compound wave are similar to the LDLR results (see [2] for details) and are not connected to the asymptotic region. Due to the compressible character of high-order schemes, the shock speed is approximated slower than the characteristic speed at some cells between the rarefaction and the shock. Adding diffusion, i.e. simply decreasing the parameter β in $\hat{\phi}$ Eq. 3.9 damps out the spurious overshoot in the vicinity of shock.

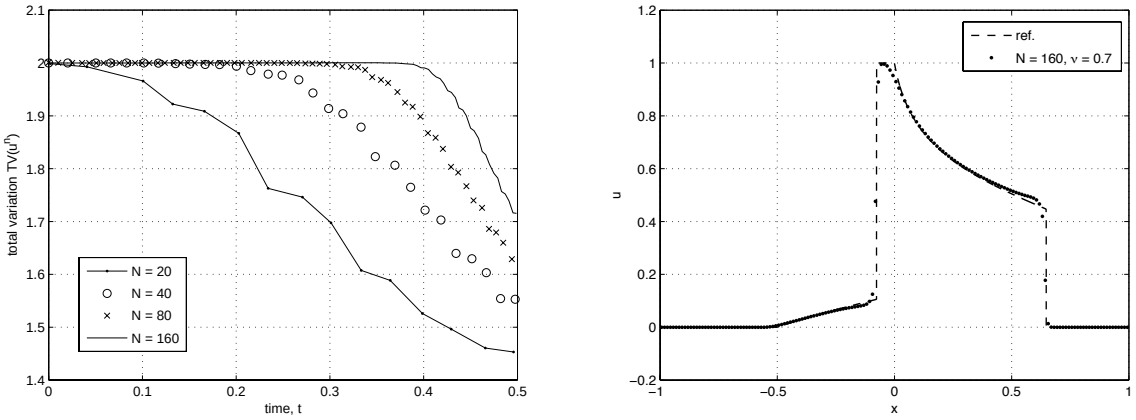

Figure 11: Total variation of Buckley–Leverett equation (left) and LimO3 approximation with $\nu = 0.7$ and $r = 0.1$ at $t = 0.4$

5.2 One-Dimensional Systems

The order of the scheme is based upon the reconstruction of the interface values and not upon the numerical flux function. Hence the proposed scheme is not tied to any particular flux function. Since our reconstruction is very efficient, we can choose a more costly –in terms of floating point operations– flux function. We formulate the numerical flux in terms of the eigenvalues all λ_p, eigenvectors r_p and characteristic variables α_p of the Roe-averaged matrix [10]:

$$\mathcal{F}_{i+\frac{1}{2}}(\hat{u}^{(-)}, \hat{u}^{(+)}) = f(\hat{u}^{(-)}) + \sum_p \alpha_p |\lambda_p| r_p. \tag{5.7}$$

All calculation are performed with the limiter function applied on conservative variables in order to keep the new method as simple and efficient as the TVD-MUSCL scheme.

5.2.1 Gas Dynamics: 1D Euler Equations

We consider a inviscid, compressible and non-heat conducting gas modeled by the Euler equations:

$$\partial_t \begin{pmatrix} \rho \\ \rho v \\ E \end{pmatrix} + \partial_x \begin{pmatrix} \rho v \\ \rho v^2 + p \\ v(E+p) \end{pmatrix} = 0, \tag{5.8}$$

where ρ is the density, p is the pressure and v is the velocity, respectively. We assume a polytropic gas with the total energy

$$E = \frac{1}{2}\rho v^2 + \frac{1}{\gamma - 1} p, \tag{5.9}$$

where γ, the adiabatic exponent, i.e. the gas constant, is set to be 1.4 for diatomic gases. We compute initial value problems by means of an initial profile of the primitive variables ρ, v, and p defined through the domain.

5.2.2 Nonlinear travelling plane waves

In order to calculate the EOC for nonlinear systems, we have chosen a nonlinearly coupled test problem, which developes a shock profile. We consider a convergence test on periodic boundaries $x \in [0, 1]$ with initial conditions

$$\begin{pmatrix} \rho \\ v \\ p \end{pmatrix}_0 = \begin{pmatrix} (1 + \frac{1}{2}(\gamma - 1)\frac{v_0}{c_0})^{\kappa} \\ 1/4 \sin(\pi x) \\ (1 + \frac{1}{2}(\gamma - 1)\frac{v_0}{c_0})^{\gamma \kappa} \end{pmatrix}, \quad c_0 = \sqrt{\gamma}, \quad \kappa = \frac{2}{\gamma - 1} \tag{5.10}$$

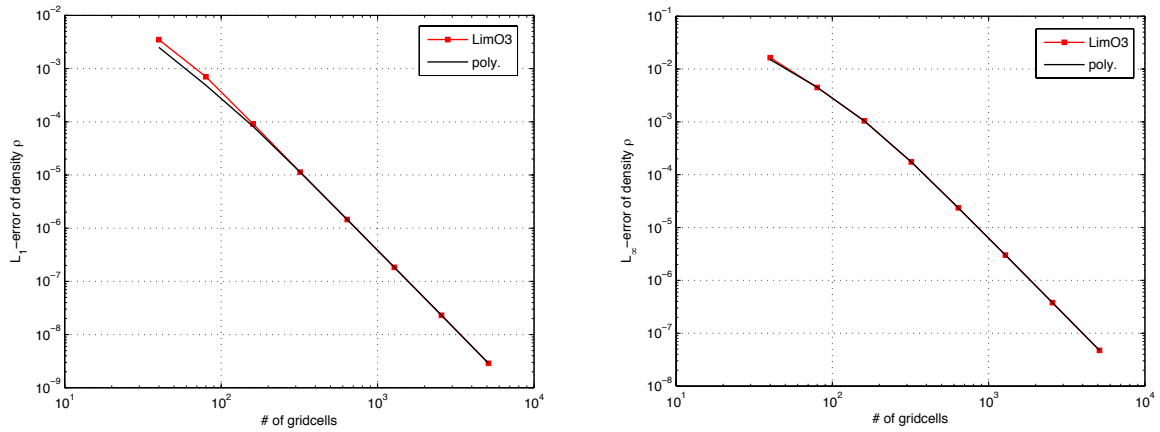

Figure 12: EOC density profile of a non-linear plane wave for the Euler equations at $t = 0.8$ with $\nu = 0.8$ and $r = 0.01$

The initially smooth flow will eventually steepen up and form a shock wave at $t^\star = \frac{8}{\pi(\gamma+1)} \approx 1.06$ [9]. This way the EOC reflects the accuracy of the whole scheme, including a linearized approximative Riemann solver.

In Fig. 12 we have plotted the calculated errors in the density component at $t = 0.8$. A reference solution is obtained with the third-order unlimited polynomial reconstruction Eq. (3.1) using 40960 cells. Due to the rather flat initial density profile we get almost optimal accuracy with already 40 computational cells.

5.2.3 Riemann Problem: Shockblast interaction

In this rather challenging problem, suggested as benchmark in [21], two blast waves collide and generate multiple strong shocks and rarefactions in the computational domain $x \in [0, 1]$. Classical second-order TVD limiters, such as superbee are either to compressive and produce negative density or they are to diffusive and smear out the contact waves and local extrema. The initial data for the simulation consist of three constant states:

$$(\rho, v, p)_0 = \begin{cases} (1, 0, 10^3) & 0 \le x < 0.1 \\ (1, 0, 10^{-2}) & 0.1 \le x < 0.9 \\ (1, 0, 10^2) & 0.9 \le x \le 0.1 \end{cases} \tag{5.11}$$

Reflecting boundary conditions are applied on both ends of the domain and the solution is evolved until $t = 0.038$ with $r = 1.0$. Fig. 13 and Fig. 14 compares the density, total energy and pressure profiles computed on a 800 cell grid with reference- and LDLR-data from [2].

The results obtained with the new scheme LimO3 with Courant number $\nu = 1.5$ approximates the solution more accurately than LDLR. In both, the density and the energy distribution we can clearly observe a better resolution of the local extrema in the middle of the domain. The shock is resolved sharp along only two cells without any spurious oscillations and with the correct velocity. The left contact discontinuity is also very accurately approximated.

5.2.4 Riemann Problem: Shock-Acoustic-wave interaction

This test case was proposed in [16]. It simulates an interaction of a supersonic shock wave with a sinusoidal density disturbance involving smooth structures and a sharp shock. A Mach 3 shock

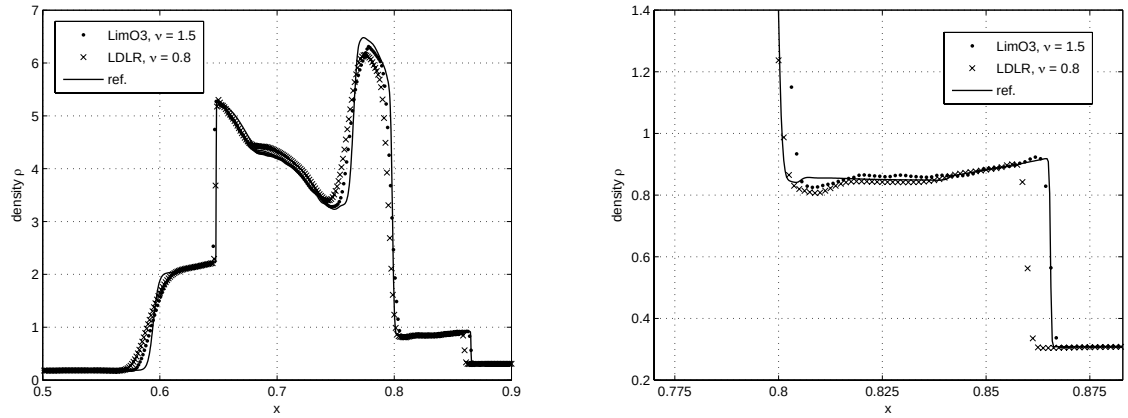

Figure 13: Density profile of shock-blast interaction problem for Euler equations. Comparison at $t = 0.038$ of LimO3 ($r = 1.0$) and LDLR ($q = 1.4$) using 800 cells.

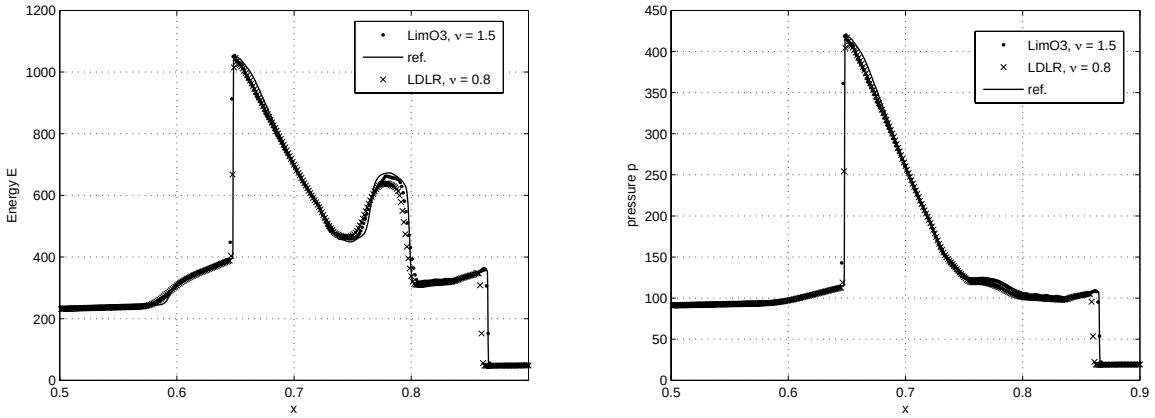

Figure 14: Energy (left) and pressure (right) distribution of shock-blast interaction problem for Euler equations. Comparison at $t = 0.038$ of LimO3 ($r = 1.0$) and LDLR ($q = 1.4$) using 800 cells.

wave moves into a smooth acoustic wave, which gets amplified and has higher frequency right behind the shock. We solve the 1D Euler equation on the domain $x \in [-5, 5]$ with constant extrapolating boundary conditions. The initial conditions are prescribed as

$$(\rho, v, p)_0 = \begin{cases} (3.857143, 2.629369, 10.333333) & x < -4 \\ (1 + 0.2\sin(5\,x), 0, 1) & x \geq -4. \end{cases} \tag{5.12}$$

In Fig. 15 we show computational results for the density component obtained at $t = 1.8$ using 400 FV-cells. We compare the solution for the proposed algorithm LimO3 with LDLR results from [2]. Since the solution is dominated by smooth, but narrow structures we have expanded the asymptotic region Eq. (3.14) setting the radius $r = 5$. Thus the local extrema in $x \in [0.5, 2]$ are considerably better resolved and perfectly symmetric. We have to note that we could also run this Riemann problem without any limiting procedure, hence using the full parabolic spatial reconstruction Fig. 16 (left). Similar to the observation we have made for the linear advection equation (see Fig. 8) the unlimited third-order reconstruction remains stable with minor over- and under-shoots in the vicinity of the shock, hence allowing us to choose a large asymptotic region. This is in contrast to classical second-order method, which could not simulate this experiment without proper TVD limiters. Yet even compressible TVD limiters, such as van

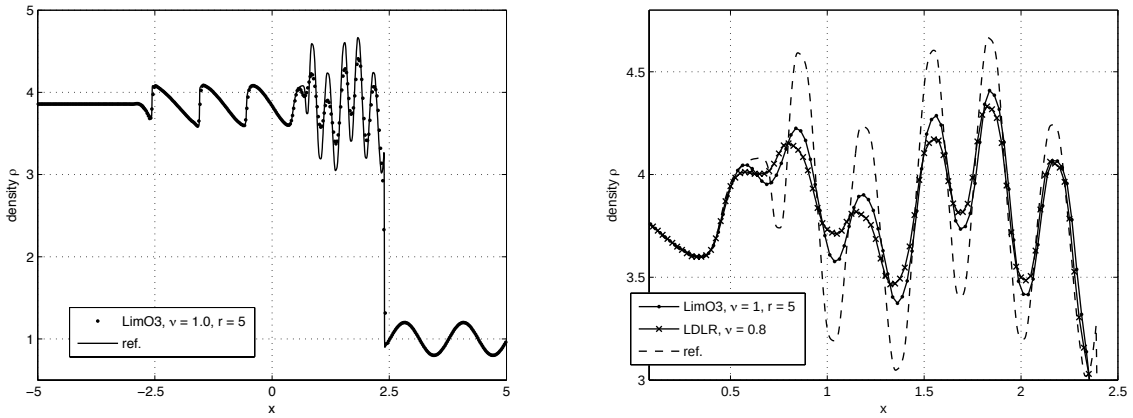

Figure 15: Density distribution of Shu–Osher shock-acoustic test case for Euler equations. Comparison at $t = 1.8$ of LimO3 ($r = 0.5$) and LDLR using 400 cells.

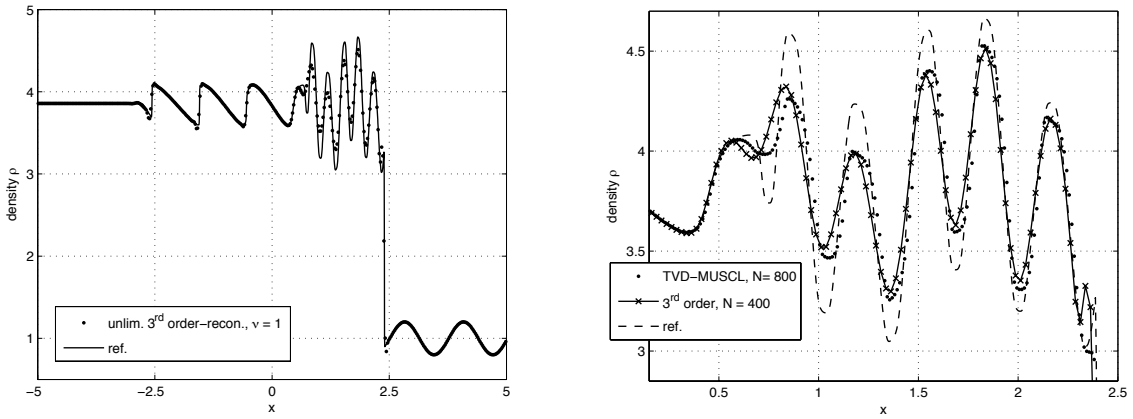

Figure 16: Density distribution of Shu–Osher shock-acoustic test case for Euler equations. Comparison at $t = 1.8$ of unlimited quadratic reconstruction Eq. (3.1) using 400 cells and second-order TVD-MUSCL scheme with van Leers' limiter with 800 cells.

Leers, need around twice as much computational cells to resolve the smooth structure behind the shock Fig. 16.

Note that if we set $r \leq 1$ we obtain qualitatively similar results as LDLR, yet we produce no undershoots in the region with steep gradients $x \in [-2, 0]$. This is an advantage of our limiting procedure, because we do not change its TVD property once a discontinuity is detected, i.e. the function $\hat{\phi}(\theta)$ is switched on. Enlarging the asymptotic region allowes, even on a coarse mesh, to consider data with large curvature as smooth structures. This is different in the LDLR scheme. There the total-variation-control-parameter q has to be decreased. This eventually leads to an improved resolution of the smooth profile in $x \in [0.4, 2.4]$, but also to more variation in the vicinity of discontinuities, because variation is introduced everywhere.

5.3 Magnetohydrodynamics (MHD)

We extend our 1D system to the ideal MHD equations, which model the dynamics of plasma. Plasma dynamics are influenced by magnetic fields induced through the Lorentz-force. Therefore an additional evolution equation for the magnetic field $\boldsymbol{B}$ has to be derived. Further terms in the

Euler system Eq. (5.8) which quantify magnetic force and energy density are also needed. The adiabatic constant is $\gamma = 5/3$. The whole MHD system including the approximative Riemann solver can be found in e.g. [19] or [20] (and references therein).

The intention of this section is twofold. First we consider a convergence test to prove the formal order of our scheme for a non-linear rather complicated system. Second we compare the non-uniform converge for one dimensional MHD Riemann problems for different schemes.

5.3.1 Empirical Order of Convergence (EOC)

We solve the MHD equations on the domain $x \in [-1, 1]$ with smooth initial data [1], $\rho = 1.5 + 0.5\sin(\pi x)$, $v_x = 1.5 + 0.25\cos(\pi x)$, $v_y = 1.5 + 0.25\sin(\pi x)$, $B_x = 0.5$, $B_y = 1.0$ and $p = 0.25$. The errors are calculated for $t = 0.628$ using a reference solution obtained on a very fine grid with the pure quadratic reconstruction Eq. (3.1). We compare the convergence rate of both LimO3 and LDLR method to envisage the particular difference of the radius r in the proposed asymptotic domain and the variation-control-parameter q of LDLR.

Fig. 17 shows the calculated empirical convergence error for the density distribution of the LimO3 scheme for various radii of the asymptotic region. In Fig. 18 we envisage the empirical convergence error of LDLR. LDLR has been implemented as described in [2]. Both methods need around 200 FV-cells to reach the desired convergence error since the smooth extrema in the density profile is rather narrow. However LimO3 converges always faster, i.e. using less grid cells, than LDLR. In addition for $r = 1.0$ and $r = 0.5$ the convergence error is clearly smaller than for LDLR with $q = 1.0$. Remember for $q \longrightarrow 0$, LDLR recovers the pure quadratic polynomial. Though the most important difference is, that even for a small radius of the asymptotic region we clearly see the correct convergence error. Whereas LDLR with the variation-control-exponent $q = 1.0$ needs more than 5000 FV-cells to converge to the error of pure quadratic reconstruction. In other words with changing the radius of the asymptotic region we just change the ability of the new limiter $\phi^{\mathcal{O}(3)}(\delta_{i-1/2}, \delta_{i+1/2})$, to distinguish between local smooth extrema or discrete gradients with one vanishing lateral derivative. But once a discontinuity is recognized the limiter $\hat{\phi}(\theta)$ diminishes total variation. Changing the variation-control-parameter q in LDLR affects the whole reconstruction procedure. A small q increases the total variation (decreases the diffusion), yet the reconstruction can not accurately recover smooth extrema with one vanishing lateral derivative. For $q > 1.4$ the total variation is significantly decreased, yet diffusion is also increased, but the LDLR algorithm can resolve smooth extrema with one vanishing lateral derivative more accurately. This is a significant difference of both schemes. Our aim is primary to retain the very good shock capturing properties of the $\hat{\phi}(\theta)$ limiter and yet to be able to accurately resolve smooth structures with one vanishing lateral derivative.

5.3.2 Pseudo-Convergence

We consider an almost coplanar Riemann problem, as proposed in [19], to investigate the convergence properties towards the true solution. It has been described in details for several second-order methods in [19] and for very high, up to a ninth-order method, in [20] that all schemes converge initially to a wrong solution. Only with a very fine spatial resolution the methods start to converge to the right solution. As such, the Riemann problem is a hard test case for FV-methods. The aim is to recover the correct convergence on a coarse computational grid.

We investage the error of the numerical solution obtained by the proposed method LimO3 and compare it to three different methods: A second-order methods (Roe2) with $\nu = 0.9$ (see [19]), a fifth-order WENO (WENO5) scheme with $\nu = 0.4$ (see [20] and references therein), and the

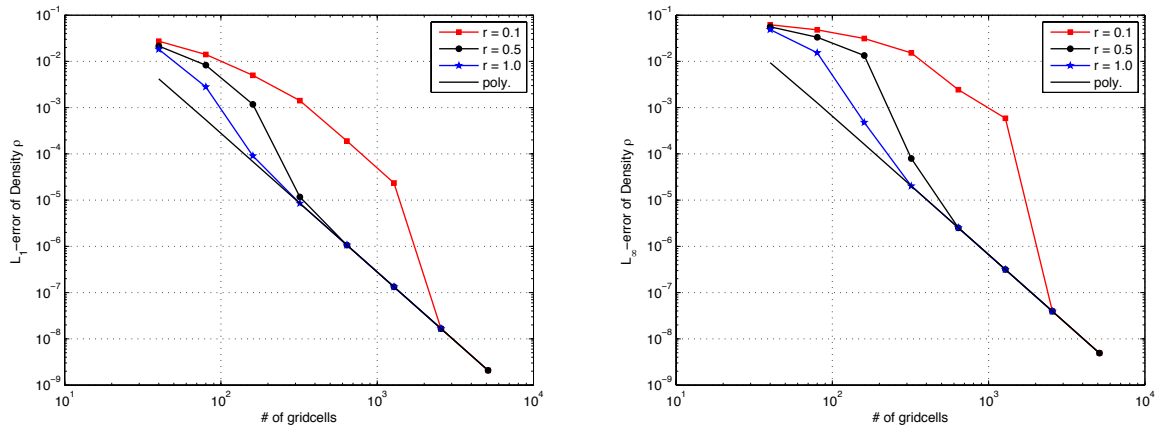

Figure 17: EOC of LimO3 for the 1D MHD-system at $t = 0.628$ with $\nu = 0.8$ and different asymptotic regions.

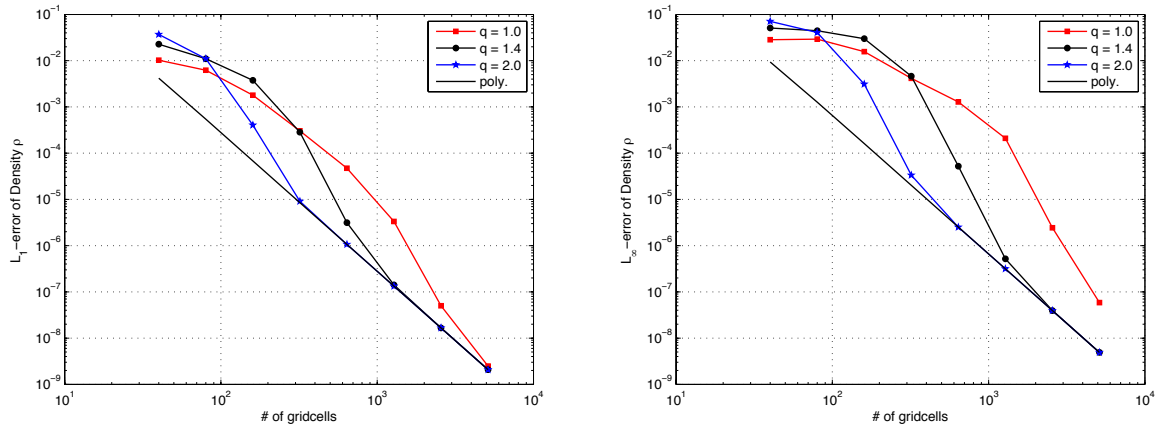

Figure 18: EOC of LDLR for the 1D MHD-system at $t = 0.628$ with $\nu = 0.8$ and different variation-control-parameter q.

LDLR method with $\nu = 0.9$. Roe2, LimO3 and LDLR are conducted with the same approximative Riemann solver and the higher-order methods, LimO3, LDLR and WENO5 use the same explicit three-stage Runge-Kutta time marching scheme. The second-order TVD Heun time marching scheme is implemented in Roe2.

The left picture in Fig. 19 shows the convergence results of the the magnetic field B_y for an almost coplanar Riemann problem consisting only of regular waves (r-solution), i.e. shock and discontinuities. The solution for the Riemann problem consisting of any non-regular waves, c-solutions for compound waves, are shown in the right picture of Fig. 19. LimO3, LDLR and WENO5 exhibit eventually the same results. All three methods start to converge with the same accuracy from 1000 cells upwards to the true solution. As already concluded in [20] very high order, such as WENO5, do not significantly improve the pseudo convergence although they display smaller numerical viscosity than second-order TVD methods (Roe2). Note that LimO3 qualitatively computes the same numerical solution as WENO5, yet using a nearly four times higher Courant number $\nu = 1.5$ and only three-data points for spatial reconstruction. Changing the radius of the asymptotic region did not improve the pseudo convergence.

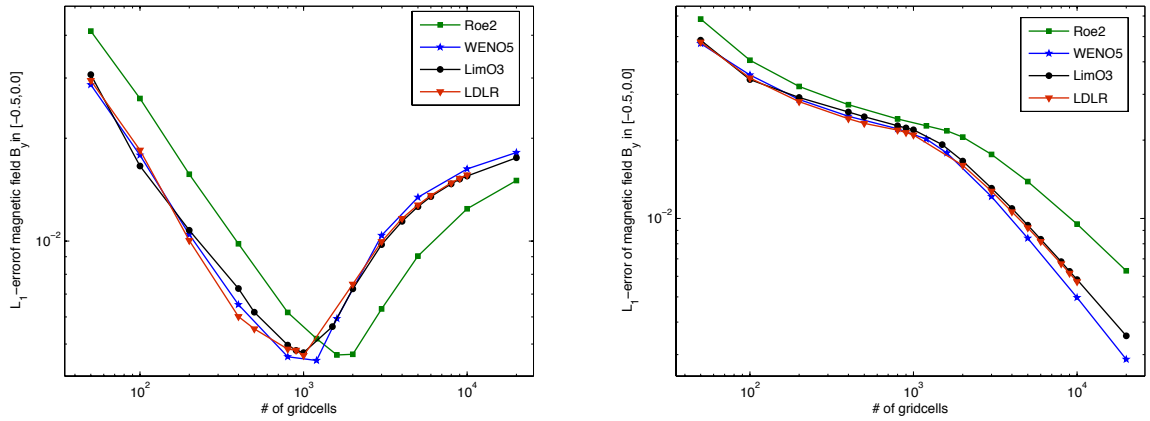

Figure 19: Almost co-planar MHD Riemann problem. L_1-errors of the magnetic field B_y for the twist angle $\alpha = 3.0$ with respect to the c-solution (left) and r-solution (right). Lim03 has $\nu = 1.5$ and $r = 0.5$.

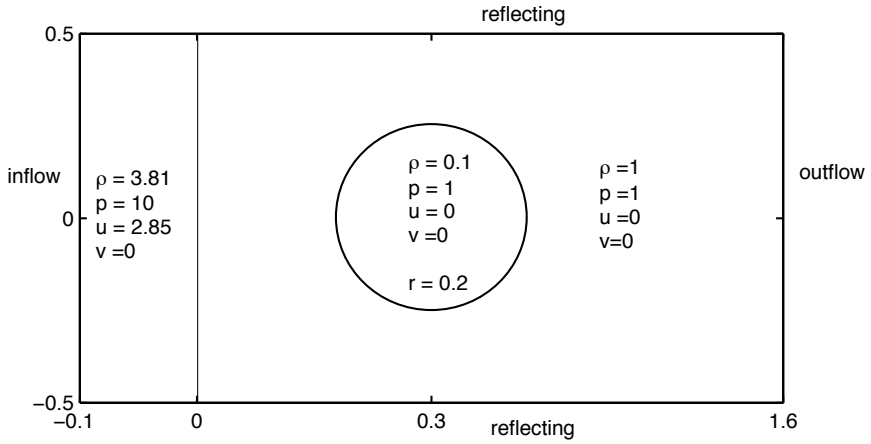

Figure 20: Shock-Bubble experimental setup for 2D Euler equation.

5.4 Euler System in Two Dimensions

We compute 2D experiments using a dimension by dimension reconstruction approach.

$$\begin{aligned} \frac{d}{dt}\bar{u}_{ij} &= L_i(\bar{u}_j) + L_j(\bar{u}_i) \\ &= \frac{1}{\Delta x}\left(\mathcal{F}_{i-\frac{1}{2},j} - \mathcal{F}_{i+\frac{1}{2},j}\right) + \frac{1}{\Delta y}\left(\mathcal{G}_{i,j-\frac{1}{2}} - \mathcal{G}_{i,j+\frac{1}{2}}\right) \end{aligned} \tag{5.13}$$

We recover the intermediate values $\hat{u}^{(\pm)}_{i\pm\frac{1}{2},j}$ and $\hat{u}^{(\pm)}_{i,j\pm\frac{1}{2}}$ with the proposed third-order reconstruction applied on the conserved variables using the HLLE approximative Riemann solver [18]. Since the flux evaluation is done in both directions in every single Euler stage of the third-order Runge-Kutta method, the stability criterion yields:

$$\nu = 0.5\,(\nu_x + \nu_y) \leq 1.6 \tag{5.14}$$

5.4.1 Shock-Bubble

In this experiment we simulate a strong rightwards moving shock wave over a low density gas bubble. The initial condition and the experiment geometry is sketched in Fig. 20. As the problem is symmetric we compute the upper part $y \geq 0$ only and specify reflecting boundary

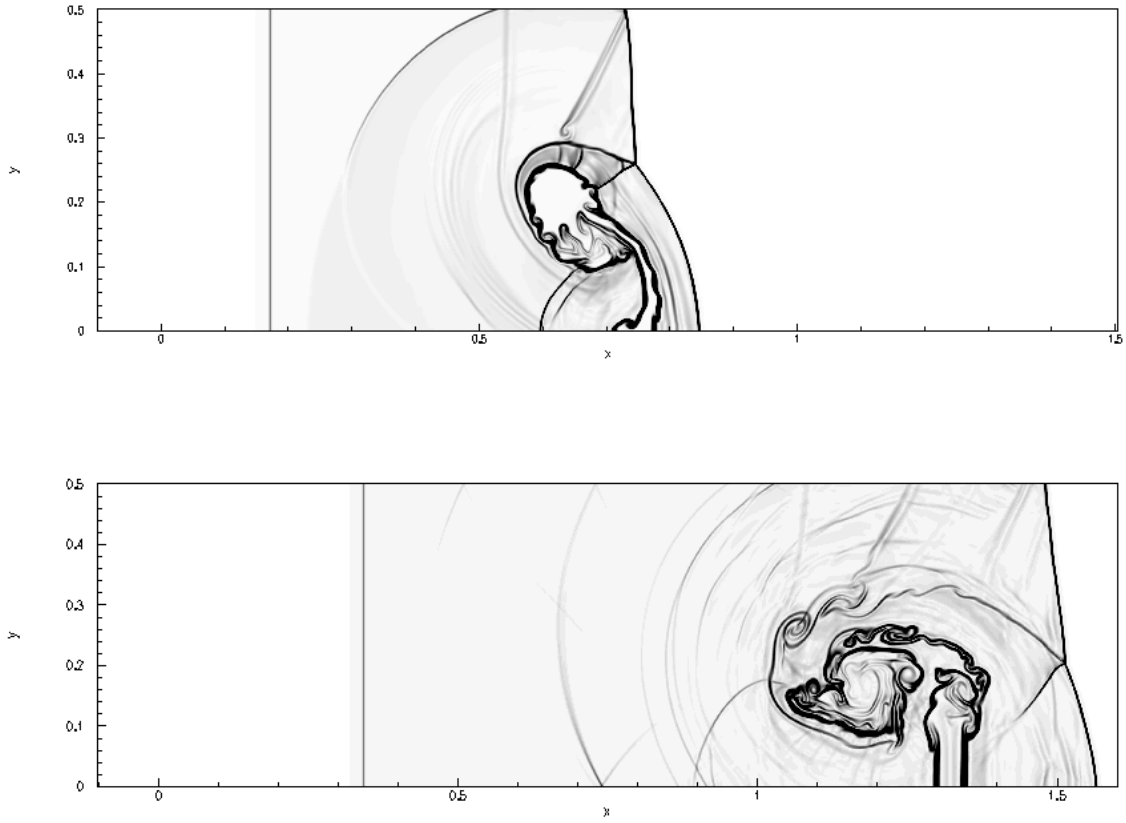

Figure 21: Emulated Schlieren picture of shock-bubble simulation with 1600×500 cells with $\nu = 1.5$. Top: $t = 0.2$. Bottom $t = 0.4$.

conditions at $y = 0$ and inflow boundary condition at $x = -0.1$.

The LimO3 and van Leer's TVD-MUSCL approximations are computed on a uniform mesh consisting of 1700×500 FV-cells. LimO3 results are obtained using $\nu = 1.5$ with $r = 1.0$, whereas the TVD-MUSCL scheme has $\nu = 0.9$, employing a second order time-marching scheme and van Leers' limiter function. Fig. 21 shows the numerical results of LimO3 at different times. The emulated Schlieren pictures display density gradients on a grey scale. In Fig. 22 the results at $t = 0.4$ are compared for both LimO3 (left) and TVD-MUSCL (right). We observe many more small scale vortexes in the approximation of LimO3. The contact discontinuities are resolved more accurately with the third-order method LimO3, yet still remaining computationally as fast as the second-order TVD-MUSCL scheme.

5.4.2 2D Riemann Problem

We have taken a 2D Riemann problem originally defined in [14]. The problem is solved on a square domain $(x, y) \in [0, 1] \times [0, 1]$, with initial constant states in four quadrants with the contact point localized at $(3/4, 3/4)$ as proposed by [15]:

$$(\rho, u, v, p)_0 = \begin{cases} (1.5, 0, , 0, 1.5) & [0.75, 1] \times [0.75, 1] \\ (0.5323, 1.206, 0, 0.3) & [0, 0.75) \times [0.75, 1] \\ (0.138, 1.206, 1.206, 0.029) & [0, 0.75) \times [0, 0.75] \\ (0.5323, 0, 1.206, 0.029) & [0.75, 1] \times [0, 0.75) \end{cases} \tag{5.15}$$

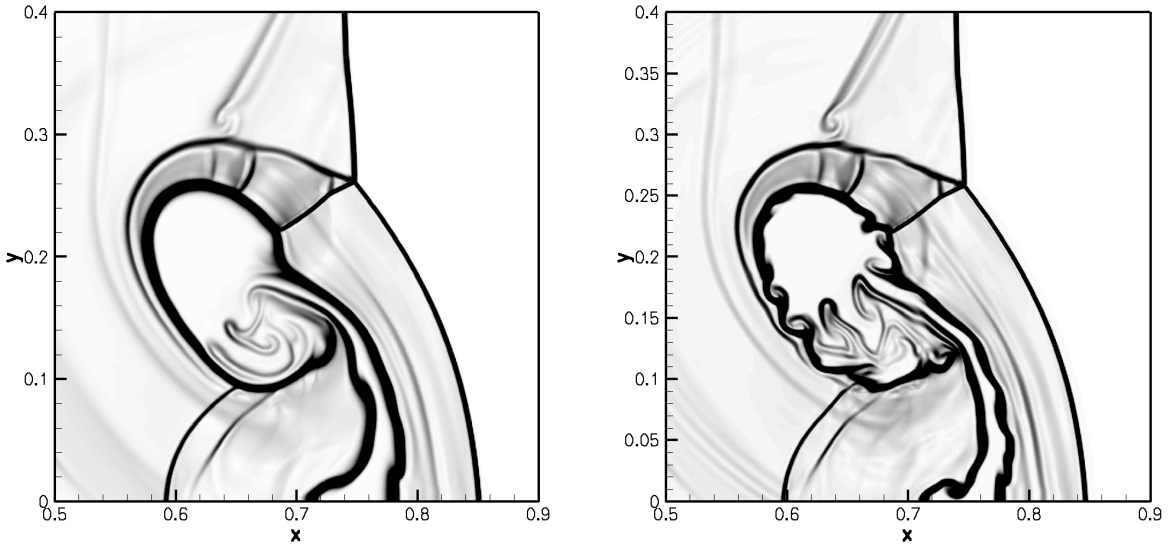

Figure 22: Zoom of the shock-bubble Schlieren image Fig. 21. Left: Second-order TVD-MUSCL scheme with van Leer limiter with $\nu = 0.9$. Right: LimO3 ($r = 1.0$) with $\nu = 1.5$

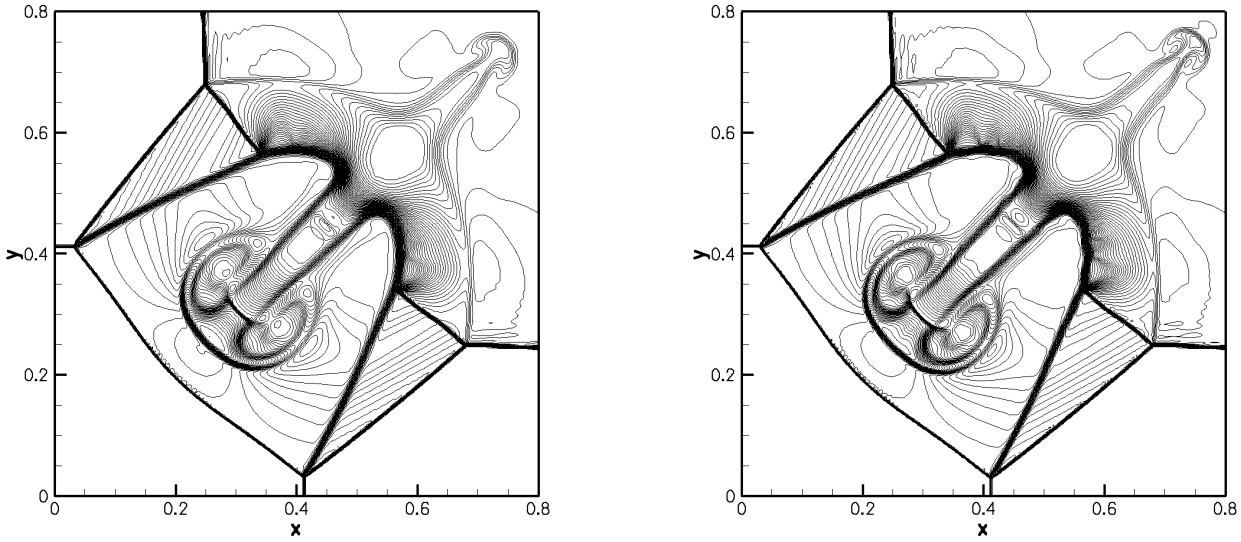

Figure 23: Density contour plot of 2-d Riemann problem using 400×400 cells at time 0.8. Left: Second-order TVD-MUSCL scheme with van Leer limiter and $\nu = 0.8$. Right: LimO3 with $\nu = 1.5$ and $r = 0.5$.

We compare in Fig. 23 density contour profiles of LimO3 and van Leers' second-order MUSCL scheme. The numerical solution is obtained at $t = 0.8$ with a Courant number of $\nu = 1.5$ for LimO3 and $\nu = 0.8$ for van Leer's TVD-MUSCL scheme on a uniform grid with 400×400 cells. All boundaries are artificial boundaries, i.e. constant extrapolated. Both approximations are of similar quality, although LimO3 resolves several structures better, such as the contact discontinuity and the middle and top right plume. The LimO3 are perfectly symmetric. Note that the LimO3 simulation is, because of Courant number $\nu = 1.5$, as fast as the second-order accurate TVD simulation, yet essentially of third-order accuracy in smooth regions.

6 Conclusions

In this paper we have derived and analyzed a new third-order limiter for the numerical solution of hyperbolic conservation laws. In contrast to classical second-order TVD-limiters, the proposed limiter function maintains its formal accuracy at local extrema. Yet remaining still a simple, efficient peacewise linear $(\max, \min)$-function. It acts as a logical switch depending on the left and right slope and avoids complicated and costly reconstruction techniques. The new limiter uses a local piecewise parabolic reconstruction for smooth data and preserves accuracy within the asymptotic region. Similarities to limiter functions obeying Harten's TVD conditions have been analyzed. The new algorithm uses, in contrast to second order methods, an explicit third-order Runge-Kutta time marching scheme. Clear advantages in the frequency domain and less restrictive conditions for numerical stability for this time marching method could be shown.

Various numerical experiments indicate the superiority of the proposed limiter over classical second-order methods TVD limiters. The new scheme also compares favorably with third-order methods such as LDLR and ENO3. It has very good shape-preserving properties and known limiter effects, such as smearing and squaring do no appear. Numerical simulations with Courant numbers up to $\nu = 1.6$ make the proposed method just as efficient as classical second-order TVD-MUSCL schemes, yet significantly improving the result. Note that TVD methods are computationally more economical than ENO schemes [16]. Costly optimal stencil searches and memory storage is avoided.

Acknowledgments

The first author thanks Robert Artebrant for many fruitful discussions about reconstruction techniques in finite volume methods and for kindly providing us with his data.

References

[1] R. Artebrant. *Reconstruction Techniques and Finite Volume Schemes for Hyperbolic Conservation Laws*. PhD thesis, Doctoral Theses in Mathematical Sciences, Lund University, 2006.

[2] R. Artebrant and H.J. Schroll. Limiter-free third order logarithmic reconstruction . *SIAM J. Sci. Comput.*, 28:359–381, 2006.

[3] M. Cada, M. Torrilhon, and R. Jeltsch. Compact Third Order Logarithmic Limiting for Non-Linear Hyperbolic Conservation Laws. In Sylvie Benzoni-Gavage and Denis Serre, editors, *Proceedings of the 11th International Conference on Hyperbolic Problems, Lyon, France*. Springer, 2008.

[4] S. Gottlieb and C.-W. Shu. Total Variation Diminishing Runge-Kutta Schemes . *Math. Comput.*, 67:73–85, 1998.

[5] A. Harten. High resolution schemes for hyperbolic conservation laws . *J. Comput. Phys.*, 59:357–393, 1983.

[6] A. Harten, B. Enquist, S. Osher, and S.R. Chakravarthy. Uniformly high order accurate essentially non-oscillatory schemes, III . *J. Comput. Phys.*, 71:231–303, 1987.

[7] H.T. Huynh. Accurate Monotone Cubic Interpolation . *Siam J. Numer. Anal.*, 30:87–100, 1993.

[8] G.-S. Jiang and C.-W. Shu. Efficient implementation of weighted ENO schemes . *J. Comput. Phys.*, 126:202–228, 1996.

[9] L.D. Landau and E.M. Lifshitz. *Fluid Mechanics*, volume 6 of *Course of Theoretical Physics*. Pegamon Press, 1982.

[10] R.J. LeVeque. *Finite Volume Methods for Hyperbolic Problems*. Cambridge Texts in Applied Mathematics, 2003.

[11] X.-D. Liu, S. Osher, and T. Chan. Weighted essentially nonoscillatory schemes . *J. Comput. Phys.*, 115:200–212, 1994.

[12] A. Marquina. Local Hyperbolic Reconstruction of Numerical Fluxes for Nonlinear Scalar Conservation Laws . *SIAM J. Sci. Comput.*, 15:892–915, 1994.

[13] S. Osher. Convergence of generalized MUSCL schemes . *SIAM J. Numer. Anal.*, 22:947–961, 1985.

[14] C.W. Schulz-Rinne, J.P. Collins, and H.M. Glaz. Numerical solution of the Riemann problem for two-dimensional gas dynamics . *SIAM J. Sci. Comput.*, 14:1394–1414, 1993.

[15] S. Serna. A class of extended limiters applied to piecewise hyperbolic methods . *Siam J. SCI. Comput.*, 28:123–140, 2006.

[16] C.-W Shu and S. Osher. Efficient implementation of essentially non-oscillatory shock capturing schemes, II . *J. Comput. Phys.*, 126:32–78, 1989.

[17] A. Suresh and H.T. Huynh. Accurate Monotonicity-Preserving Schemes with Runge–Kutta Time Stepping . *J. Comput. Phys.*, 136:83–99, 1997.

[18] E.F. Toro. *Riemann Solvers and Numerical Methods for Fluid Dynamics 2nd edition.* Springer, Berlin, Germany, 1999.

[19] M. Torrilhon. Non-uniform convergence of finite volume schemes for Riemann problems of ideal magnetohydrodynamics . *J. Comput. Phys.*, 192:73–94, 2003.

[20] M. Torrilhon and D.S. Balsara. High order WENO schemes: investigation on non-uniform convergence for MHD Riemann problems . *J. Comput. Phys.*, 201:586–600, 2004.

[21] P. Woodward and P. Colella. The numerical simulation of two-dimensional fluid flow with strong shocks . *J. Comput. Phys.*, 54:115–173, 1984.

[22] P. Woodward and P. Colella. The piecewise parabolic method (PPM) for gas-dynamical simulation . *J. Comput. Phys.*, 54:101–136, 1984.

A Derivation of the Logarithmic Limiter

In order to derive the logarithmic limiter Eq. (3.6) we have to formulate the cell interface values of LDLR as function of the smoothness measurement θ Eq. (2.8). The mesh size independent cell interface values of the LDLR are given by:

$$\hat{u}_{i\pm1/2}^{(\mp)} = \bar{u}_i + c\,\eta^{(\pm)}(a) + d\,\eta^{(\pm)}(b) \tag{A.1}$$

Where a, b, c and d are explicit function of the left and right slope [2]:

$$\begin{aligned} a(\delta_{i-1/2}, \delta_{i+1/2}) &= 1 - 2\frac{|\delta_{i-1/2}|^q\,|\delta_{i+1/2}|^q}{|\delta_{i-1/2}|^{2q} + |\delta_{i+1/2}|^{2q}} \\ &= 1 - 2\frac{|\theta|^q}{1+|\theta|^{2q}}, \quad \delta_{i+1/2} \neq 0 \end{aligned} \tag{A.2}$$

We define a function depending solely on the slope ratio θ (see Eq. (3.7))

$$p = p(\theta) \equiv 1 - a \tag{A.3}$$

The functions b, c and d are algebraic expressions of $a(\delta_{i-1/2}, \delta_{i+1/2})$ and the left and right slopes. The logarithm functions come into the reconstruction via the functions [2]:

$$\begin{aligned} \eta^{(+)}(z) &= -\frac{\ln(1-z)+z}{z^2} \\ \eta^{(-)}(z) &= \frac{(z-1)\,\ln(1-z)-z}{z^2} \end{aligned} \tag{A.4}$$

We can reformulate all these functions in terms of θ and $p(\theta)$:

$$b = \frac{a}{a-1} = \frac{p-1}{p} \tag{A.5}$$

$$c = \frac{(a-1)(\delta_{i+1/2}(1-b) - \delta_{i-1/2})}{b-a} = \frac{p-\theta\,p^2}{1-p^2}\delta_{i+1/2} \tag{A.6}$$

$$d = \delta_{i-1/2} - c = (\theta - \frac{p-p^2\theta}{1-p^2})\delta_{i+1/2} \tag{A.7}$$

$$\begin{aligned} \eta(a)^{(+)} &= -\frac{\ln(p)+1-p}{(1-p)^2} \\ \eta(a)^{(-)} &= \frac{(-p)\,\ln(p)-1+p}{(1-p)^2} \end{aligned} \tag{A.8}$$

To recover Eq. (3.5) with a single logarithmic limiter function Eq. (3.6), we have to plug in the above equations into Eq. (A.1) and extract once the right ($\delta_{i+1/2}$) and the left ($\delta_{i-1/2}$) slope.